Limpet-inspired design and 3D/4D printing of sustainable sandwich panels: Pioneering supreme resiliency, recoverability and repairability

Saman Jolaiy [a,1], Armin Yousefi [a,1], Mohsen Hosseini [a], Ali Zolfagharian [b], Frédéric Demoly [c,d], Mahdi Bodaghi [a,*]

[a] Department of Engineering, School of Science and Technology, Nottingham Trent University, Nottingham NG11 8NS, UK
[b] School of Engineering, Deakin University, Geelong, Victoria 3216 Australia
[c] ICB UMR 6303 CNRS, Belfort-Montbeliard University of Technology, UTBM, Belfort 90010, France
[d] Institut Universitaire de France (IUF), Paris, France

ARTICLE INFO

ABSTRACT

Sandwich panels, characterized by their solid exterior and thick, soft core, find extensive applications ranging from maritime to aerospace sectors due to their exceptional resilience and energy absorption/dissipation capabilities. The natural limpet, known for its resilience to mechanical loading, serves as inspiration in the present research to introduce innovative repairable core shells. Limpet-inspired shells with elasto-plastic and brittle behaviors are designed and 3D/4D printed using polylactic acid (PLA) filaments and resins via fused filament fabrication (FFF) and liquid crystal display (LCD) techniques. While PLA filament exhibits an elasto-plastic response with a shape-recovery feature, the resin results in brittle structures for LCD-printed design. The study demonstrates that the FFF-printed PLA shell can fully recover residual plastic deformations, while the LCD-printed PLA shell exhibits a mechanical fracture behavior very similar to the natural limpet with brittle properties. A nonlinear finite element model (FEM) is also developed to replicate the large deformations of the samples under quasi-static compression with a high level of accuracy. Experimental and numerical results reveal that the samples with material, mechanical behavior, and geometry close to the natural limpet result in the maximum energy dissipation per unit mass. Two bio-inspired cores are then tessellated to introduce a new class of sustainable sandwich panels with supreme recoverability, resiliency, and repairability. A three-point bending test is numerically carried out on sandwich panels using FEM, and their energy absorption and dissipation capacities are studied. Results demonstrate that the proposed sandwich panels can achieve almost 7.33 and 1.17 times higher energy dissipation per unit mass than those developed based on a recycled thermoplastic bottle cap core. This pioneering research sets a new benchmark for structural design in terms of resiliency, recoverability, repairability, and sustainability.

1. Introduction

The unique architecture of sandwich panels imparts outstanding mechanical performance under various loading conditions, including low-velocity and high-velocity impact, as well as bending loading. Comprising three main layers, i.e., the solid upper and lower face sheets and the thick, soft inner core, sandwich panels, usually assembled by adhesive, boast mechanical properties such as high bending stiffness, lightweight, significant impact resistance, and considerable energy absorption/dissipation capabilities. Consequently, they find applications in the automotive, marine, and aerospace industries [1–3].

The material and architectural complexity of sandwich panels have evolved to meet the growing demands for enhanced structural integrity, aerodynamic properties, thermal insulation, and acoustic performance across many engineering applications [4–6]. Core architecture and materials have been identified as crucial factors influencing the multifunctional performance of sandwich structures [4,7,8]. Therefore, the core structure plays a crucial role in determining the overall performance of sandwich structures [9]. Several studies have investigated the mechanical behavior of sandwich structures with different core shapes,

both numerically and experimentally, such as honeycombs [2], corrugated [10], chiral structure [11], tetrahedral truss [12], Y-frame [13], and double cell wall square [14]. Other studies have explored the impact of different core materials, including Nomex [2], foam [15], and aluminum alloy [16], on the mechanical performance of sandwich structures.

Many attempts have been made to design and manufacture different forms of sandwich panel cores, tailoring engineering demands by the emergence of novel manufacturing techniques including additive manufacturing (AM), often known as 3D printing. AM has accelerated the growth of sandwich structures with complex core shapes and allows for the creation of inner cores with intricate configurations, which is almost impossible using conventional fabrication methods. AM presents outstanding advantages, including the ability to manufacture intricate structures, cost-effectiveness, and time-saving processes [17–20]. The remarkable potential of AM has attracted significant attention to manufacturing various sandwich panels in response to growing industry demands. For instance, two novel composite structures with hexagonal and square horseshoe unit cells were manufactured by 3D printing technology and tested [21]. Experimental and numerical results show the remarkable energy absorption of these composite structures. The effect of core thickness and 3D printing parameters, such as layer height, on sandwich structures' energy absorption and compression strength was investigated numerically and experimentally. Hedayati et al. [22] proposed a novel type of sandwich panel with different patterns of truncated cube unit cells to achieve a higher energy absorption to weight ratio, known as specific energy absorption (SEA). The proposed sandwich panels can be repaired by replacing the damaged unit cells. Sarvestani et al. [4] evaluated the mechanical performance of 3D-printed sandwich panels with architected cellular cores of programmable six-sided cells using analytical, numerical, and experimental tools. Low-velocity impact tests were conducted to investigate the energy absorption capability of proposed sandwich structures. Results show the 3D-printed sandwich panels with architected cellular cores have high energy absorption capability, making them a potential candidate for energy absorption applications.

Recent achievements in AM have introduced a novel paradigm known as 4D printing, endowing printed structures with shape recovery and shape morphing features in response to external stimuli, including heating [17,23–27]. Structures produced via 4D printing can recover their initial shape after being deformed through a simple heating-cooling process. This capability is used to design and manufacture a new class of sandwich structures with recoverability properties [21]. Noteworthy applications of 4D printed shape memory structures include boat fender meta-structures with considerable energy absorption capability, showcasing the potential of these structures for practical use [17].

One of the most promising approaches for designing structures with high energy absorption/dissipation capability is to mimic the nature. Biological materials and structures have evolved and adapted for millions of years in response to their harsh environments such as high-impact loads to survive. Engineers are inspired by this adaptation to design, optimize, and fabricate new types of materials and structures, tailoring engineering demands, for example, inspiring from the nature to design an inner core with good impact resistance feature for optimizing the performance of sandwich panels, known as bioinspiration [18,25, 28–32]. Recent studies [28,33–37] have investigated the mechanical performance of sandwich structures with bio-inspired inner cores, leveraging the development of 3D/4D printing technology. Cui et al. [38] proposed a novel design inspired by the microstructure of the cuttlebone. The bio-inspired cuttlebone-like sandwich structure's compression resistance and energy-absorbing capacity were examined. The selective laser melting (SLM) method was employed to prepare the bio-inspired sandwich structures. Results reveal that bio-inspired cuttlebone-like sandwich structures can potentially be used in protective energy-absorbing components in the aerospace and medical industries.

Le et al. [39] examined the fracture mechanisms of 3D-printed corrugated-core sandwich composite structures inspired by beetle forewing made of carbon fiber-reinforced polymer under bending load. Employing digital image correlation (DIC), the load capacity, compressive strengths, and failure mechanism were investigated under quasi-static and compression tests. Results indicate that the proposed bio-inspired sandwich structures offer a significant bending stiffness-to-weight ratio. Another study on bio-inspired sandwich structures, conducted by Hu et al. [28], examined four lightweight sandwich structures inspired by the microstructures of the Norway spruce stem. Sandwich structures were printed using SLM. The uniaxial compression tests were conducted to examine the designed structures' compressive strength and energy absorption capability. Results show that the gradient structure developed based on tube-like unit cells, with tube size (inner core shape) gradually decreasing from the top and bottom panels towards the core, has the highest specific absorption energy. This study indicates the importance of a functionally graded core, where the core structure's geometry varies in particular directions for mechanical properties of structures, such as energy absorption.

By reviewing open literature, it is acquired that increasing energy absorption/dissipation capability while maintaining the structure's weight as low as possible is one of the primary objectives of designing sandwich panels. Meanwhile, no attention has been given to developing a sandwich panel that provides resilience, recoverability, and repairability, all-in-one design, to reduce maintenance and replacement costs while maintaining considerable energy absorption/dissipation capability. This feature becomes even more vital when durability is essential, and replacement is a formidable task, as seen in devices such as the Mars rover. Resilience is another critical parameter, defined as the ability of materials or structures to absorb impact energy and still recover their initial shape.

In this context, the present study focuses on designing a novel bio-inspired shell with considerable energy dissipation capability, supreme resiliency, recoverability, and repairability, an all-in-one design by mimicking natural limpet structures. According to the available data, the limpet life span varies, but it is almost ten years. Limpet shells serve as protective shields and prevent dehydration for limpets when they are out of the water [40]. Comprising almost entirely calcium carbonate, with a small percentage of organic matter [41], limpet shells exhibit notable toughness, almost ten times higher than calcium carbonate in its mineral state, leading to extensive research endeavors to develop bio-inspired materials based on their structures [40,42]. In the present study, the limpet-inspired shell is designed based on average dimensions reported in the literature for limpets, with three different thicknesses. Two different techniques are employed for the 3D printing of bio-inspired shells. Subsequently, a quasi-static compression test is conducted, and the force-displacement response is documented for all samples. Utilizing a finite element method (FEM), the mechanical response of unit cells is numerically simulated in a quasi-static manner. A comparison is made between the mechanical performance of bio-inspired unit cells and the mechanical testing outcomes of quasi-static compression of 3D-printed samples. Energy dissipation per unit mass, known as specific energy dissipation (SED) is reported for all samples. The proposed design, distinguished by its superior energy dissipation capability, establishes the groundwork for the development of sandwich panels including various arrays of limpet-inspired unit cells, characterized by recoverability, and an easy-to-repair feature. Additionally, SED as crucial parameters to design sandwich panels is determined for all samples.

Fig. 1 illustrates the overall structure of the present research. The first step involves defining the problem: designing a novel energy-dissipating structure inspired by the nature with considerable resiliency, recoverability, and repairability. The natural limpet adaptation, where both energy absorption and mass are highly crucial, serves as inspiration. A novel limpet-inspired shell is designed (step 2). The bio-inspired shell is then 3D printed, with its mechanical properties
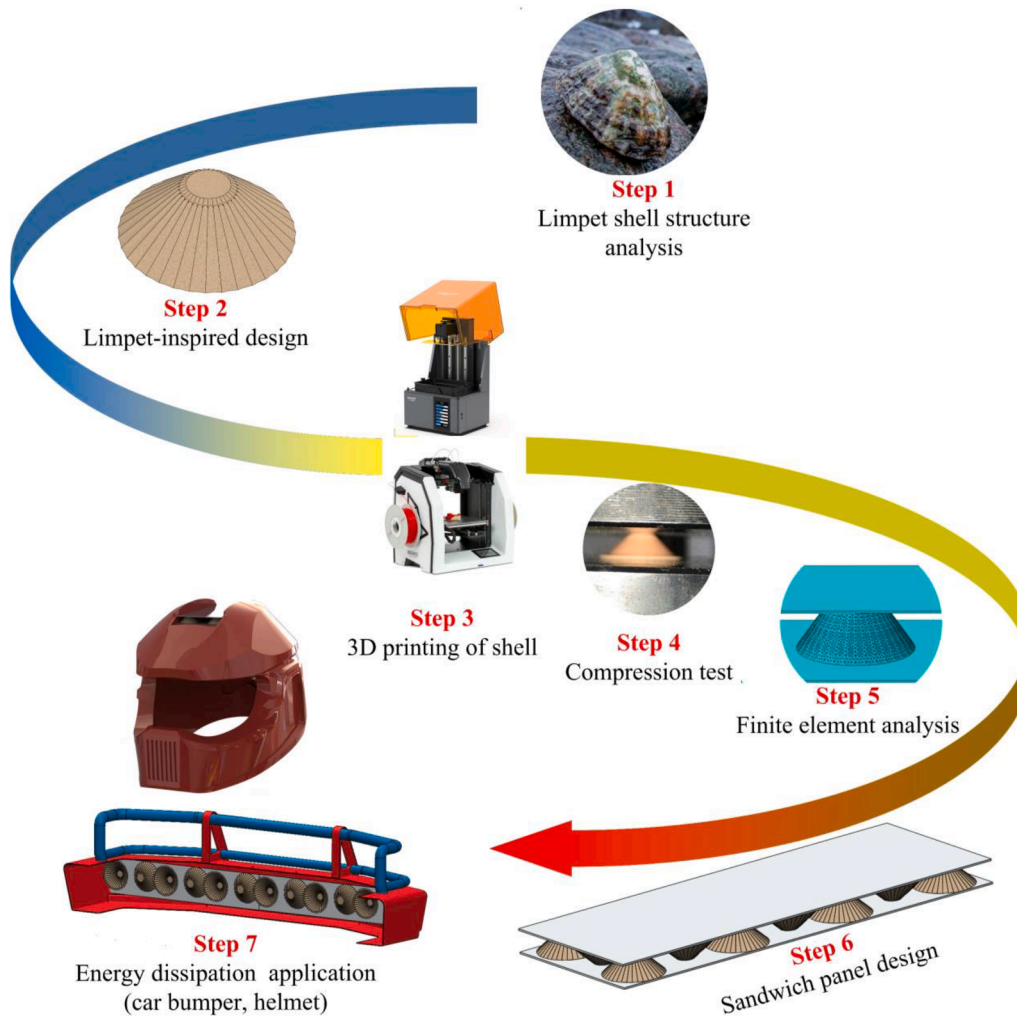
Fig. 1. The overall process, from bio-inspired design, modeling, and 3D/4D printing to analysis and application.

determined numerically and experimentally (steps 3, 4, and 5). Based on the supreme energy dissipation capability of the limpet-inspired shell, the sandwich panel is created (step 6), demonstrating an easy-to-repair feature with a wide range of applications, such as car bumpers, helmets, and boat fender applications (see step 7).

2. Design, manufacturing, and experimental setups

2.1. Conceptual design

A recent study by Vafidis et al. [43] focuses on the Patella caerulea limpet shell discovered in the Eastern Mediterranean (Central Greece). The picture of a natural limpet shell is presented in Fig. 2. The

approximate dimensions related to the limpet shell are listed in Table 1. In Table 1, t stands for shell thickness which varies from 0.943 to 1.663 mm.

The computer-aided design (CAD) software SOLIDWORKS® (Dassault Systems, France, version 2022) was used to define the geometry of the bio-inspired limpet shells (see Fig. 3). In this figure, D_1, D_2, H, and t_1 represent the upper and lower shell diameters, height, and shell

Table 1
Dimensions of limpet according to Vafidis et al.'s study.

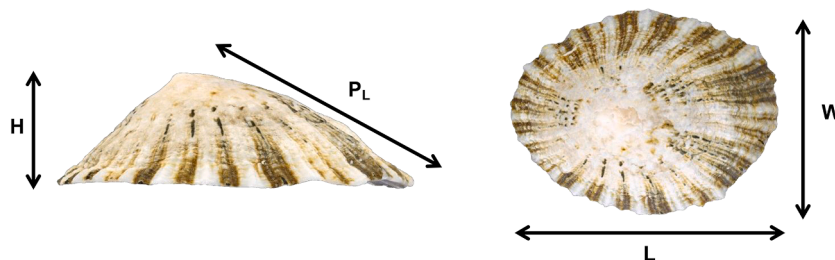| L (mm)	W (mm)	P_L (mm)	H (mm)	t (mm)
21.322–25.14	17–19	9.7–11.21	5.2–6.22	0.943–1.663

Fig. 2. Dimensions of a limpet shell discovered by Vafidis et al. [43]: shell length (L), shell width (W), shell height (H), and posterior shell length (P_L).
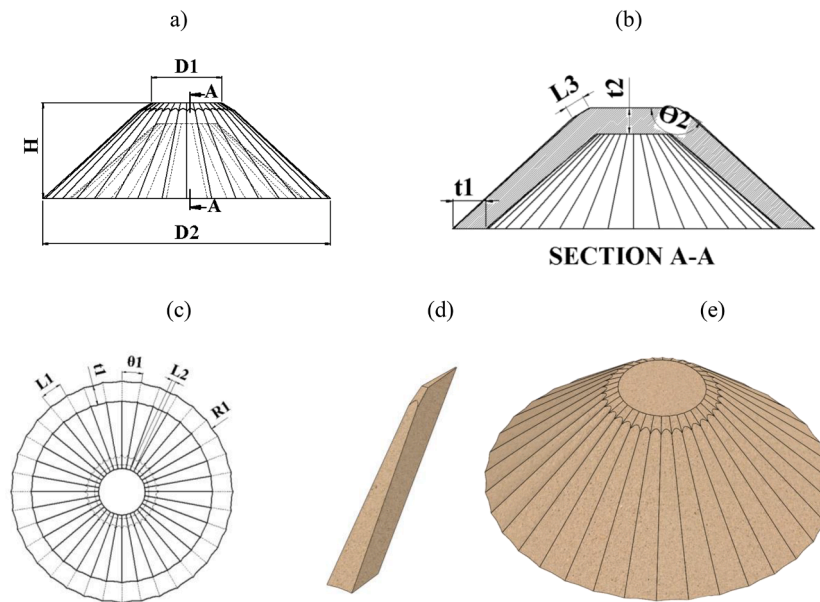
Fig. 3. Developed bio-inspired design based on the limpet shells: (a) side view, (b) cross-section, (c) top view,(d) an oblique cylindrical section, and (e) realistic rendering.

thickness, respectively. While t_2 is the thickness between the top plane and the bottom plane. The parameter that denotes the thickness of the shell is a crucial parameter in the study of limpet shells and is significant in determining the shell's structural integrity and mechanical properties. Therefore, measuring and analyzing the thickness of the limpet shell is a crucial aspect of current research. Moreover, L_1, L_2, L_3, Θ_1, Θ_2, and R_1 stand for the down distance, upper distance, the length of the upper fillet, the angle between each costa (ridges), the angle between the top surface and each costa, and the lower edge's radius of curvature, respectively. An oblique cylindrical section was created, as presented in Fig. 3d, with dimensions listed in Table 2. The final model is created using a circular pattern of oblique cylindrical sections, as presented in Fig. 3e. In the current research, three samples with different shell thicknesses (t_1) are considered to investigate the effect of thickness on the mechanical behavior of samples. Moreover, each sample is printed using two different AM techniques. Sample geometry dimensions are listed in Table 2.

2.2. Manufacturing

What makes the current design even more viable is its manufacturing capability by different methods, including AM, casting, forging, and severe plastic deformation (SPD) due to the simple geometry of the design. Fused filament fabrication (FFF) technique was used to create the desired sample layer by layer. For this purpose, the sample was first modeled by the CAD software, exported in STL format, and imported to Cura, an open-source slicing application for 3D printers, and then imported to the 3D printer. Here, samples (A-C) were prepared by the FFF 3D printer (3D Gence Double P255, Poland) fed by polylactic acid (PLA) filaments (Recreus Inc., Elda, Spain). The printing layer height was set to 0.1 mm. The nozzle's working temperature and bed temperature were set to 215 °C, and 25 °C, respectively.

Esun photo-curable PLA resin, which was developed for liquid crystal display (LCD) printers and optimized for UV curing at 405 nm wavelength, was used for printing samples (D-F). The printer was an LCD 3D printer (HALOT-SKY: 8.9″ Large Mono LCD), which uses a 2K LCD screen (2560 × 1620 pixels) to mask an image of a layer over a UV light source, with a build volume of 119 × 65 × 160 mm and a fill density of 100 %. Fig. 4a presents PLA samples printed by FFF, and Fig. 4b shows samples printed by LCD. Eighteen samples, three samples for each material type, were printed according to ASTM D638–14 (type V) standard. The stress-strain curve of dog bone samples printed by FFF and LCD is shown in Fig. 4c. All mechanical properties related to samples are listed in Table 3.

2.3. Experimental setups

A quasi-static test entails evaluating how a limpet-inspired shell absorbs energy when subjected to axial loads that compress it. These tests are conducted with a universal testing machine, crushing the specimen at a very slow speed between two parallel jaws. The quasi-static test presents the force response, failure displacement, and energy absorption capability of the limpet-inspired core at the lower strain rate. The results give valuable insight into the mechanical behavior and performance of these structures under controlled loading conditions. These results help a better understanding of the structure's mechanical properties, such as stiffness, strength, energy absorption capacity, and resilience which are crucial for various engineering applications, including aerospace, automotive, sport and healthcare. Also, in order to analyze the recoverability of a limpet-inspired core, in the first step, the quasi-static compression test is conducted.

It should be mentioned that quasi-static compression tests do not fully capture the dynamic loading conditions that the sandwich's cores might experience in real-world scenarios, such as sudden impacts or
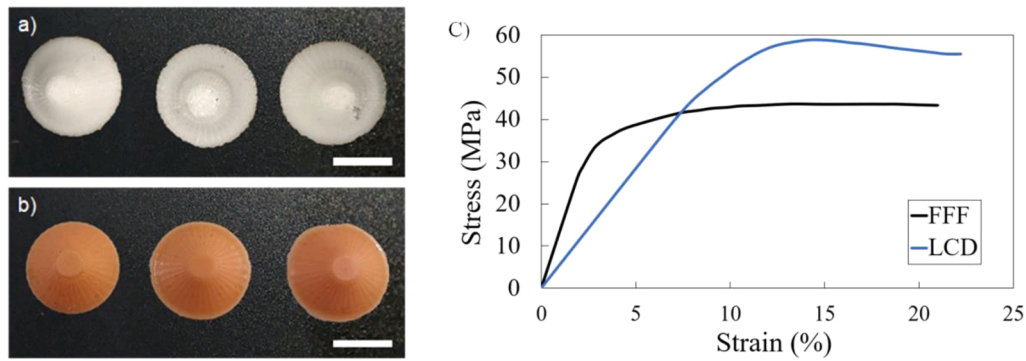
Table 2
Dimensions of bio-inspired limpet shells.

	D_1 (mm)	D_2 (mm)	H (mm)	t_1 (mm)	t_2 (mm)	L_1 (mm)	L_2 (mm)	L_3 (mm)	Θ_1 (deg)	Θ_2 (deg)	R_1 (mm)
Samples A, D	4.4	18	6	0.8	0.6	1.57	0.38	1	10	140	5
Samples B, E	4.4	18	6	1.6	1.2	1.57	0.38	1	10	140	5
Samples C, F	4.4	18	6	2.4	2.2	1.57	0.38	1	10	140	5

Fig. 4. PLA limpet shell printed using (a) FFF technique, (b) LCD technique, and (c) stress-strain curve of FFF and LCD printed samples. All scale bars: 10 mm.

Table 3
Mechanical properties of printed samples.

	Young's modulus (MPa)	Ultimate stress (MPa)	Elongation (%)	Fracture energy (J/mm^2)
PLA (FFF)	1368	43.70	17.80	–
PLA (LCD)	567	58.27	12.34	1.02

vibrations. Additionally, quasi-static tests can be time-consuming, especially for complex geometries, and may not provide insights into the structure's behavior under dynamic or high-rate loading conditions. However, this study carries on with quasi-static tests and pay the way for further investigations in the future.

The quasi-static compressive tests were conducted utilizing the Universal Testing Machine, WDW-300E model, CLASS 1, with a 2 mm/min displacement rate. First, specimens were prepared and then placed between two rigid jaws that can apply compressive loads evenly across the structure. The compressive loads were applied to the specimens using a universal testing machine. The loading was applied gradually and uniformly to avoid sudden failure. The cameras were positioned perfectly to record the compression test and present the location in which the fracture happened. Force-displacement curves were directly acquired from the machine, and the force-displacement curves were determined by averaging values for each specimen group (three specimens for each sample). After conducting each experiment the upper and lower jaws were completely clean to have the same conditions for all samples, such as the same friction between samples and jaws. After the test, limpet-inspired specimens were examined to assess any damage, deformation, or failure that occurred during testing.

Fig. 5 presents the experimental setups; the limpet-inspired shell is placed between the movable upper jaw and the fixed lower jaw.
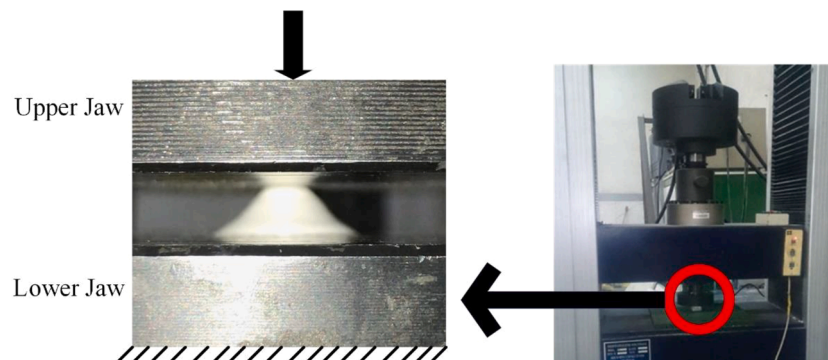
3. Numerical modeling

3.1. Mesh

A commercial non-linear FEM software package, ABAQUS (version 6.14, Dassault Systems, France), is used to accurately simulate the mechanical loading responses of 3D-printed limpet-inspired structures. CAD models created in SOLIDWORKS® software are then imported into the ABAQUS software. The calibration option within ABAQUS is utilized to import experimental stress-strain data for accurately assigning mechanical properties. ABAQUS software precisely fits the curve to the imported data, determining the mechanical properties of materials with a more precise and reliable approach. In this study, an elastic-plastic model is considered to examine the mechanical behavior of limpet-inspired shells under compression loading conditions for all samples. The dynamic implicit, quasi-static analysis is employed to simulate the mechanical behavior of the structure under compression loading conditions. It is essential to consider geometric nonlinearity by choosing the NLgeom (non-linear geometry) option in step modulus.

Fig. 6a depicts the meshed geometry of limpet-shaped unit cells, consisting of three parts: the upper movable plate, the unit cell, and the fixed lower plate. Both upper and lower plates are defined as rigid bodies in the interaction modulus within ABAQUS. Reference points are defined for upper and lower plates to capture the upper plate stroke and reaction force. General contact is defined between different parts in the normal direction, hard contact is specified, and the penalty model with a friction coefficient of 0.75 is considered in tangential directions. The mesh refinement technique is conducted to obtain more reliable outcomes while minimizing computing time. Fig. 6b presents the mesh refinement technique findings for sample F. The results show that decreasing the approximate global size to 0.3 mm leads to convergence of the force-displacement curve, so 0.3 mm is chosen for all simulation efforts. The upper and lower plates are meshed with an element type of C3D8R, an 8-node linear brick, and the limpet shell element type is a
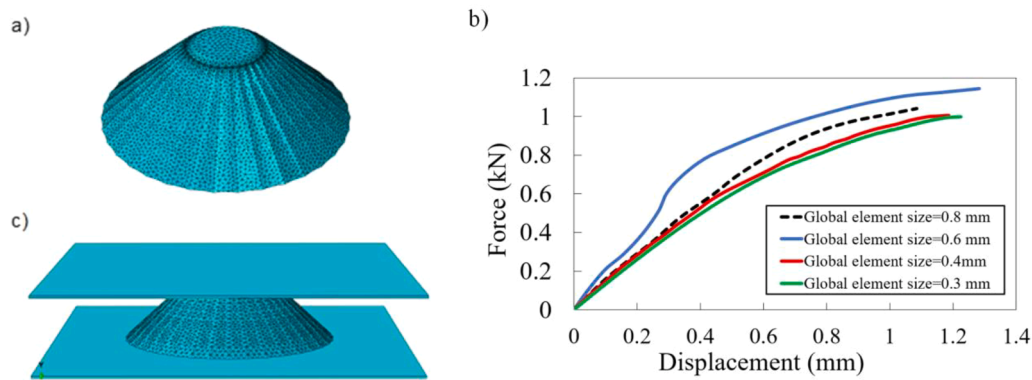

Fig. 5. The compression test setups for limpet-inspired unit cells.

Fig. 6. (a) Meshed limpet shell, (b) mesh refinement technique, and (c) overall geometry of the simulation.

linear tetrahedron of type C3D4 reduced integration. Fig. 6c presents the simulation arrangement for all samples.

4. Results

This section presents numerical and experimental findings concerning PLA limpet-inspired shells during the compression loading phases for both AM techniques.

4.1. Experimental and numerical results for samples A, B, and C

This section presents simulations and experimental results for samples A-C. Fig. 7a and b depict sample A's initial and deformed shapes, respectively. Fig. 7c and d present a FEM of sample A's initial and deformed shapes. According to the stress counter, the maximum stress occurred at the edge of the structure, where the crack was consistent with experimental observations. As evident in Fig. 7b and d, the deformed structure exhibits a bump in the center of the limpet structure. Fig. 7e presents clearly different stages of the force-displacement curve based on the experiment, which helps to better analyze the experimental results for all samples. Fig. 7e shows the force-displacement response of limpet-inspired design exhibiting elastic-plastic behavior. Several main regions, including linear region, plateau, and densification regions are identified which are broken down as follows:

1. **Elastic region:** Initially, the material deforms elastically under applied load, demonstrating linear behavior on the force-displacement curve. This stage represents reversible deformation within the material.
2. **Yield point:** Upon surpassing the yield strength, plastic deformation begins. The force-displacement curve deviates from linearity, signifying the onset of plasticity. The yield point marks the transition from elastic to plastic deformation.
3. **Plastic deformation:** Following the yield point, the material undergoes a plastic deformation. The force-displacement curve continues with a lower slope as the material experiences a plastic deformation. It is worth mentioning that shape memory polymers can recover their original shapes by external stimuli such as simple heating and plastic deformations are reversible.
4. **Plateau region:** A plateau region may emerge after initial plastic deformation. During this phase, the force remains relatively constant or fluctuates slightly while displacement rises. This plateau is often associated with mechanisms such as strain hardening or the rearrangement of polymer chains within the polymer.
5. **Densification:** Beyond the plateau region, further loading may lead to densification within this structure. Densification involves a reduction in the limpet-inspired void volume due to compaction under high pressure. This region may not always be distinct but can occur as the structure approaches its ultimate compression limit.

The force-displacement response is shown in Fig. 7f. Based on the experimental observations, global buckling occurs in the plane between the upper and lower surfaces (see Fig. 8). Also, moving further down the upper jaw results in a second buckling at the plane coincident with the inside top plane. Fig. 7f displays the simulation's force-displacement curve (black dashed line) and experiments (blue line). Based on the stress-strain curves of the PLA dog bone samples printed with the FFF technique, an elastic-plastic behavior with an extended plateau region in the force-displacement curve is expected for samples A–C. It is worth mentioning that ductile damage is not defined for samples printed with the FFF technique, as cracks initiate after densification. According to experimental results, the limpet-inspired shell undergoes linear hardening at the start of loading until a stroke of 0.5 mm. Subsequently, softening behavior occurs (from 0.5 mm to 1.25 mm), reaching the first peak force, followed by a decrease in force due to global buckling. By moving down the upper jaw, the unit cell experiences secondary hardening, with force increasing to a displacement of 1.5 mm. Following softening behavior, the force reaches 0.43 kN until the stroke of 2.8 mm, after which a nearly linear increase in force occurs until densification at 4.45 mm, where the force is 0.58 kN. At this point, the inside surface, highlighted by the blue color in Fig. 8, contacts the lower jaw, and the force increases dramatically with a slight increase in stroke; the structures lose their ability to dissipate energy. In this compression test, the force-displacement curves have two peaks since the buckling happens two times in two different planes, in the middle plane between the top and bottom surfaces and also in the plane coincident with the inside top plane (see Fig. 8), resulting in pond shaped deformation (see Fig. 7b). It is worth mentioning that the force-displacement curve of the shell from the stroke of 0.5 mm to the stroke of 4.45 mm can be considered a plateau region, and the structure dissipated energy due to plastic deformation of the shell. The simulation predicts the force-displacement curve close to the experimental study. Mechanical behavior presented by experimental study (softening-hardening behavior) is predicted by simulation. The maximum difference between the force indicated by FEM and experiments is almost 27 %. The FEM predicted the stroke in which densification occurs in the structures with reasonable accuracy, almost at the stroke of 4.5 mm.

Fig. 9a and b show sample B's initial and deformed shapes, respectively, captured from experimental observation. Fig. 9b illustrates the global buckling that occurs in the middle plane, between the bottom and top surfaces. Fig. 9c and d demonstrate the deformation the simulation predicted for the bottom and top views, respectively. Simulation shows the same behavior for the limpet-inspired shell. Both the FEM and the experiment show that the deformed structure has a bump in the center of the limpet structure. Also, according to the stress counter, the maximum stress occurs at the edge of the structure, while the crack does not initiate in sample B.

Fig. 9e displays the force-displacement curve of both the simulation and experimental investigations. According to experiential results, the
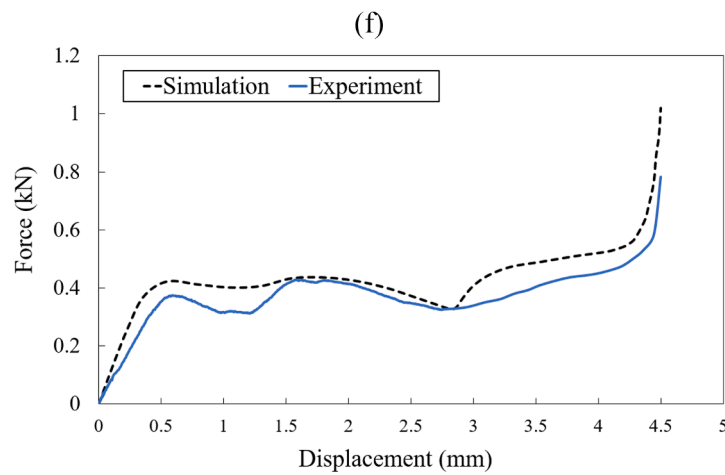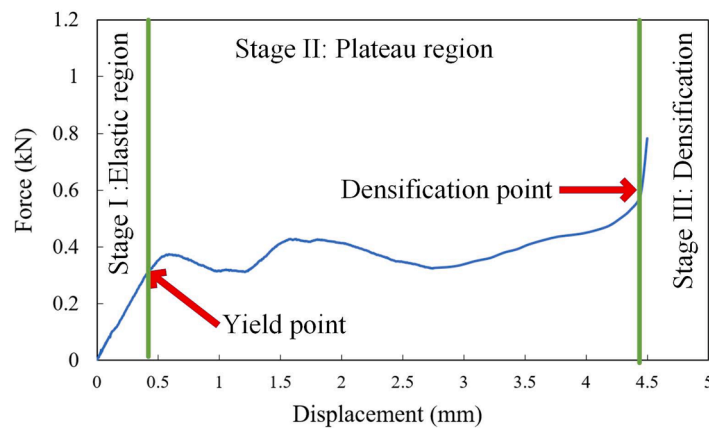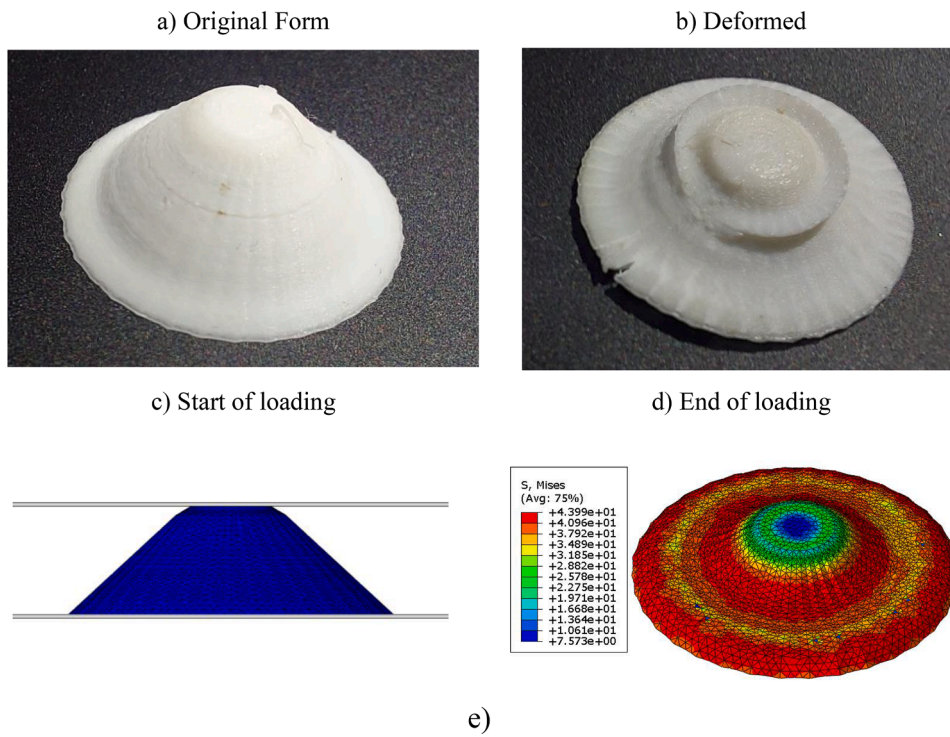
a) Original Form

b) Deformed

c) Start of loading

d) End of loading

e)

(f)

Fig. 7. Sample A (a)–(d) experimental and FEM configuration, (e) different stages of the experimental force-displacement curve, and (f) force-displacement curve for loading condition.
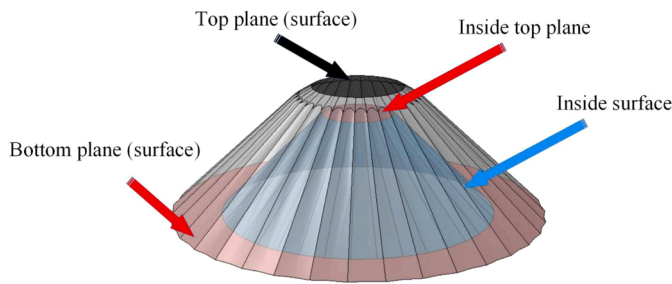
Fig. 8. Different planes and surfaces in the limpet-inspired design.

shell experiences a linear hardening at the start of loading until the stroke of 0.5 mm; the force has an increasing trend against the vertical displacement. After that, the structure experiences softening behavior (from 0.5 mm to 1.6 mm); first, the load reaches 0.50 kN at a stroke of 0.72 mm. Then, the force decreases with increasing displacement due to buckling in the structure. By moving down the upper jaw, the unit cell experiences secondary hardening behavior, in which the force increases by increasing the displacement until it reaches 2 mm. Following the shell experience, the softening behavior continues until the stroke of 4 mm.

Then, densification happens, with force increasing drastically by moving down the upper jaw at the stroke of almost 4.04 mm, where the force is 0.47 kN, in which the structures lose their ability to dissipate energy. The simulation of force-displacement agrees well with the experimental study. All mechanical behavior presented by experimental analysis is predicted by simulation, while local hardening is not predicted by simulation. This could be due to geometric imperfection in the structures fabricated by 3D printing, while FEM simulation assumes a perfect model with no inconsistencies; also, as the printed limpet dimensions are small (the bottom diameter is almost equal to 1-cent coin), geometric imperfection can have a significant impact on the force amount. According to FEM, the force-displacement curve predicted by simulation has an initial linear behavior; following softening behavior, the force reaches its maximum amount of 0.58 kN at the stroke of 1.08 mm, following the force decreases with increasing displacement until densification happens in the structure at the stroke of almost 4 mm.

Fig. 10 is the counterpart of Fig. 9 for sample C, a shell with a thickness of 2.4 mm. As shown in Fig. 10b, the deformed structure has almost a flat upper plane, which is also demonstrated by FEM (see Fig. 10c and d). It is worth mentioning that cracks in the structures happen after densification. Also, based on the experimental observations, buckling occurs two times in the structures, first on the plane near
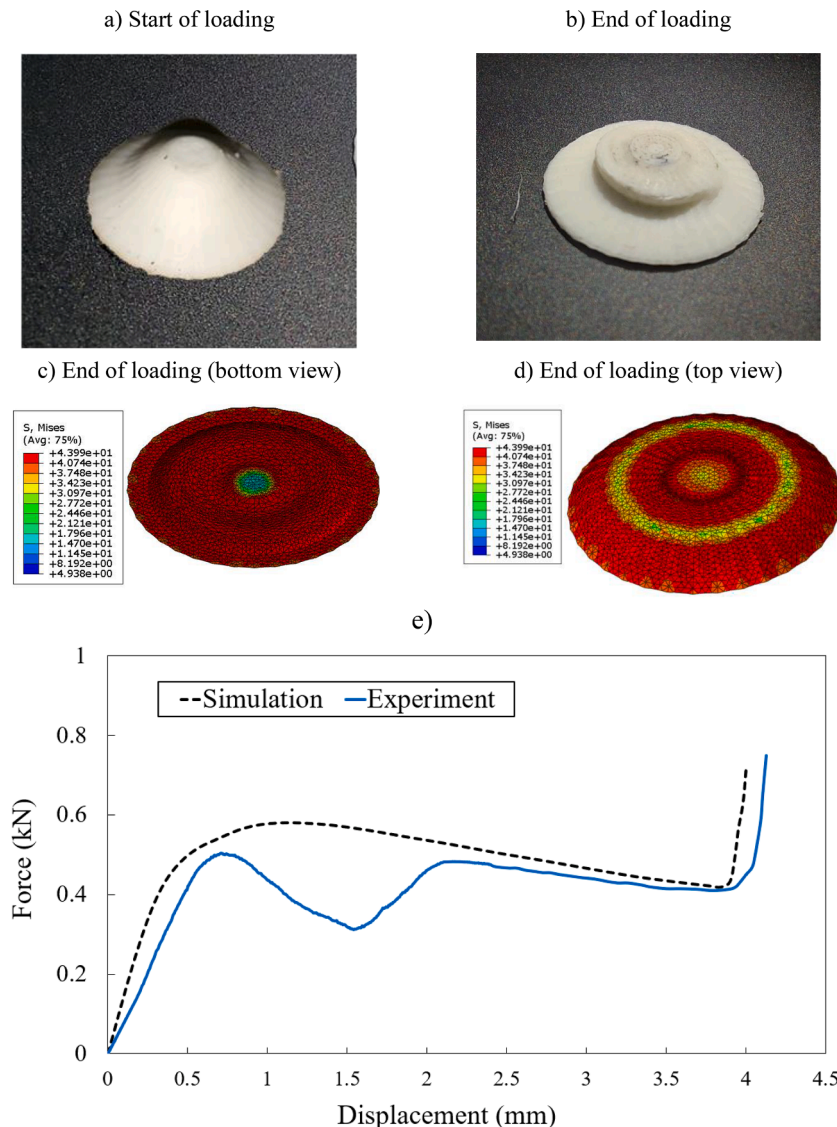

Fig. 9. Sample B (a)-(d) experimental and FEM configuration, and (e) force-displacement curve for loading condition.

a) Start of loading

b) End of loading

c) End of loading (bottom view)

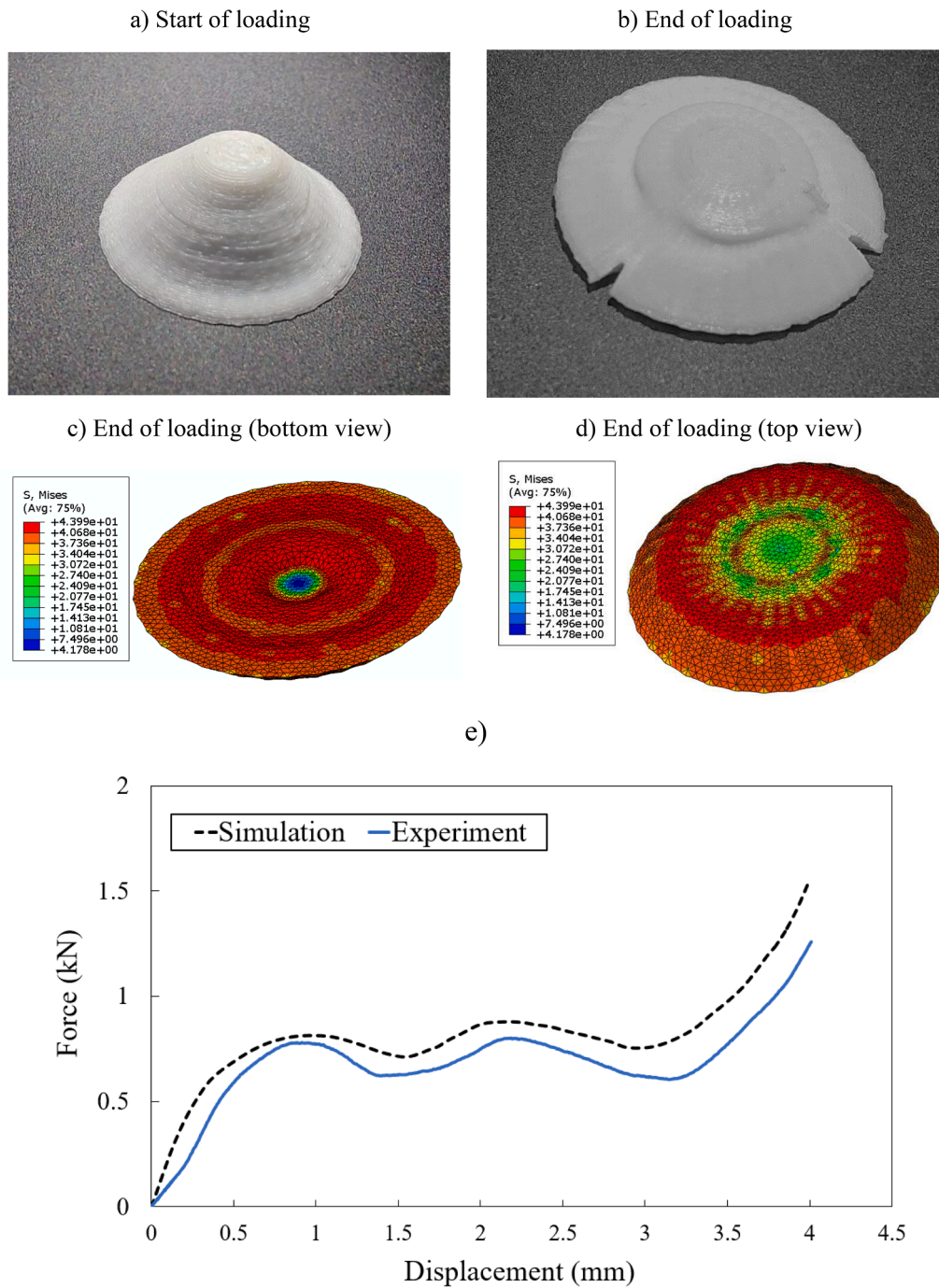d) End of loading (top view)

e)

Fig. 10. The counterpart of Fig. 9 for sample C.

the top surface, exactly the plane that is coincident with the inside top surface, surfaces, and planes are well-defined in Fig. 8, and second time in the middle plane between the top and bottom surface.

Fig. 10e draws the force-displacement curve for both simulation and experimental investigation. The experiential force-displacement curve shows that the limpet-shaped structure experiences a linear hardening; the force increases linearly with increasing displacement at the start of loading until the stroke of 0.5 mm. Then, a transient behavior from hardening to softening is observed, and the force reaches its first peak (force of 0.78 kN), following the force decreasing with increasing displacement due to the local buckling. By further moving down the upper jaw, the unit cell experiences the hardening behavior, that the force increases by increasing the displacement; the force reaches its

second peak, 0.8 kN, at the stroke of 2.2 mm. Following the shell experiences, the softening behavior continues until the stroke of 3.25 mm. Then, the force increases almost linearly by increasing stroke until densification happens in the structures at the stroke of almost 3.9 mm, and the force reaches its maximum amount of 1.10 kN. The densification occurs at a lower stroke, compared to samples A and B, as the structure has a higher thickness, so by moving down the upper jaw, the inside surface (see Fig. 11) makes contact with the lower jaw at the lower displacement compared to samples A and B, and the structures become denser, and densification happens. The force-displacement region of the shell from the stroke of 1 mm to the stroke of 3.9 mm can be considered a plateau region, and the structure dissipated energy due to plastic deformation of the shell.
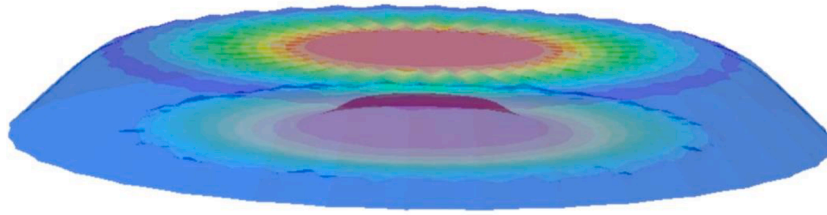
Fig. 11. The FEM model of the deformed form of Sample C with a transparent view.

The FEM force-displacement curve for sample C has good agreement with the experimental results. The FEM force-displacement curve shows that force versus displacement has a linear trend at the initial loading condition. Following the structure, it experiences softening behavior from a stroke of 0.5 mm to 1.7 mm, and force reaches a maximum amount of 0.81 kN at a stroke of 0.95 mm. Then, the force decreases by moving the upper jaw down. By further moving down, the local buckling happens for the second time in the middle plane, the softening behavior

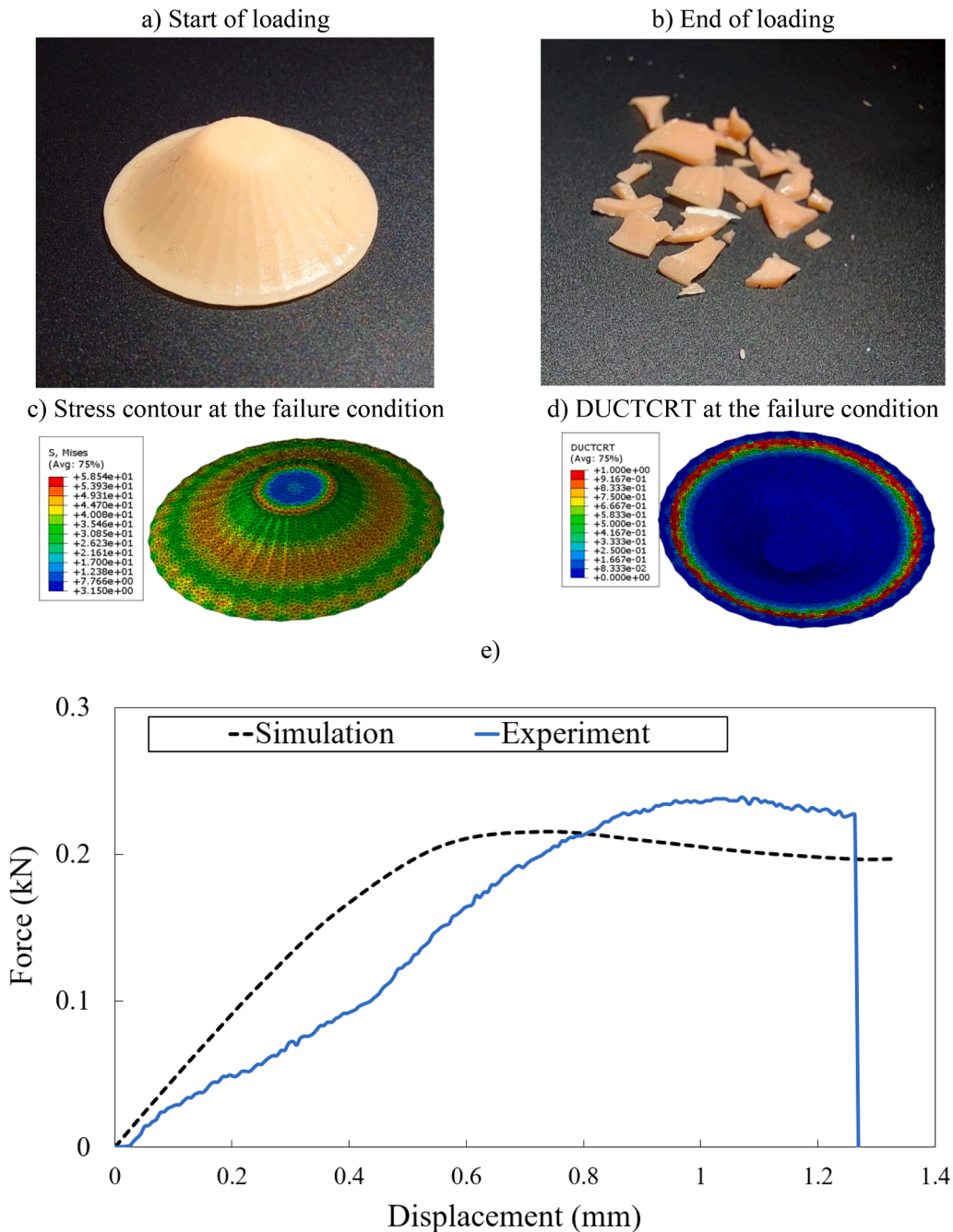a) Start of loading

b) End of loading

c) Stress contour at the failure condition

d) DUCTCRT at the failure condition

e)

Fig. 12. Sample D (a)–(d) experimental and FEM configuration, (e) force-displacement curve for loading condition.

is experienced, and the force reaches the amount of 0.85. At a stroke of almost 3.9 mm, force reaches the maximum amount of 1.41 kN; densification happens due to contact between the inside surface and the defined rigid plate. The preliminary conclusion drawn from Figs. 7 to 10 is that ABAQUS with material setting calibrated via simple tensile tests (dog bone samples) can successfully replicate deformation and force-displacement behaviors of the limpet-inspired shell with acceptable accuracy even under large strains with a low rate.

4.2. Experimental and numerical results for samples D–F

In this section, the mechanical behavior of PLA samples printed by the LCD technique is investigated both numerically and experimentally. One of the main reasons for printing the limpet-inspired shell with the LCD method is to investigate the effect of material type on the mechanical behavior and energy absorption capability of the proposed bio-inspired design. The natural limpet shell has brittle properties; the limpet shell deforms slightly before fracture [44,45]. Based on the stress-strain curve of LCD-printed dog bone specimens, the printed specimens slightly deform plastically before the fracture happens. Increasing the curing time in LCD printing makes the printed structures more brittle [46]. The ductile damage option in ABAQUS is considered to model damage in limpet-inspired shells. In order to define ductile damage in ABAQUS, the fracture strain, fracture energy for the damage evaluation (the portion of fracture energy corresponding to damage evaluation), and stress triaxiality (for pure tension, 0.33) must be specified. The upper jaw is moved downwards until a fracture occurs in the limpet shell. The ductile damage initiation criterion (DUCTCRT) is the criterion that takes into account the unit cell's damage initiation. DUCTCTR ranges from 0 to 1; when the amount of each element reaches 1, the damage is initiated, and that element loses its loading-carrying capability. The ABAQUS stops running when the fracture completely occurs due to defining damage evaluation in ABAQUS.

First, results regarding sample D, a 3D-printed PLA limpet-shaped unit cell using the LCD method for the thickness of 0.8 mm, are discussed. Fig. 12a and b illustrate the initial and final shapes of the structures. Fig. 12b shows that the structure is completely fractured. Fig. 12(c) presents the stress contour in the unit cell exactly at the failure displacement. The unit cell experiences global buckling at the middle plane, between the upper and lower planes. Fig. 12d shows the DUCTCRT, which is the criteria to demonstrate the location of damage initiation. In this unit cell, the DUCTCRT value of elements near the edge reaches 1, so the fracture initiates at this location. Therefore, the damage initiates in the lower part, and the unit cell is shattered.

Fig. 12e demonstrates the force-displacement curve for both FEM and the experimental study for sample D. The experimental force-displacement curve shows a transient behavior from hardening to softening at the initial stage of loading until the stroke of almost 0.5 mm. A hardening behavior is observed in which the force increases significantly by increasing the displacement from a stroke of 0.5 mm to 0.8 mm. In the next stage, a softening behavior occurs. First, the force reaches 0.24 kN at the stroke of 1.07 mm, and then the force decreases by moving down the upper jaw until the stroke of 1.26 mm. Then, the fracture happens by further moving down the upper jaw; the force decreases drastically, and the unit cell shatters. Safety should be considered when replicating the same experiments with the same materials, as broken parts can lead to serious damage. The FEM force-displacement curve experiences linear behavior at the start of loading until displacement of 0.4 mm. By further moving down the upper jaw, force-displacement experiences softening behavior. The force reaches the maximum amount of 0.22 kN at a stroke of 0.73 mm, then decreases with increasing displacement until the stroke of 1.3 mm, at which the fracture happens. The maximum force withstood by sample A is 160 % higher than sample D, which has the same geometry and different mechanical properties according to experimental results.

Fig. 13 presents the simulations and the experimental results of

sample E, a PLA 3D printed limpet-inspired shell using the LCD method for the thickness of 1.6 mm. Fig. 13a and b show the structures' initial and final form. Fig. 13b shows that the structure is completely fractured, and the crack path is radial from the top view of the unit cell. Fig. 13c presents the stress contour in the unit cell exactly at the displacement before a fracture occurs. The unit cell experiences buckling in the plane, which coincides with the inside top plane. Fig. 13d shows the DUCTCRT counter for sample E. In the plane coincident with the inside top plane, the DUCTCET reaches 1, and the crack initiates at the top plane of shall and propagates in the radial direction between two ridges.

Fig. 13e shows the force-displacement curve for both the simulation and experimental study of sample E. The experimental force-displacement curve shows a linear hardening behavior at the initial loading stage until the stroke of almost 0.6 mm. A softening behavior is observed in which the force increases to the maximum amount of 0.80 kN at the displacement of 1.24 mm, and the following force decreases significantly by increasing the displacement from 0.6 mm to 1.8 mm. A hardening behavior occurs by increasing displacement, in which the force increases by moving down the upper jaw until the stroke of 2.1 mm, leading to the emergence of the second pick in the force-displacement curve. Then, further moving down the upper jaw produces a softening behavior until the fracture occurs, the force decreases drastically, and crack growth. The force-displacement curve predicted by FEM is in good agreement with the experimental study. The maximum difference between forces is almost 20 %, which happened at the fracture point. The force versus displacement has a linear trend at the start of loading. The softening behavior is observed at a stroke of almost 0.7 mm, and then the force reaches its maximum amount of 0.75 kN at a stroke of 1.7 mm. The FEM predicts that the fracture occurs at a displacement of 1.7 mm, while the experiment result shows that the fracture occurs at a displacement of 2.4 mm. Experimental results show that sample E's maximum force is 60 % higher than sample B, the sample with the same geometry but different mechanical properties, which is the only sample printed by the LCD technique and still withstands higher force than the sample with the same geometry and printed by the FFF technique.

Fig. 14 is a counterpart of Fig. 12 for sample F, a PLA 3D-printed limpet-inspired shell using the LCD method for a thickness of 2.4 mm. Fig. 14b shows that the structure is completely fractured, and the crack path is radial from the top view of the unit cell, the same as in sample E. Fig. 14c presents the stress contour in sample F; the unit cell experiences the buckling at the plane coincident with inside top plane. So, the stress in this plane reaches its maximum amount. Fig. 14d shows the DUCTCRT counter for sample F. In the plane coincident with the top plane, the DUCTCET reaches the maximum amount, and the fracture initiates here. Cracks propagate along the limpet ridges until they reach the bottom plane (see Fig. 14b).

Fig. 14e demonstrates the applied load to the unit cell versus stroke until fracture. The experimental force-displacement curve shows a linear behavior at the initial loading stage until the stroke of almost 0.6 mm, even though the hardening behavior is observed at the start of loading (stroke of 0 to 0.1 mm). A softening behavior is followed by further moving down the upper jaw, pending the maximum force of 0.96 kN at the displacement of 1.1 mm; at this stage, the fracture occurs, the force decreases drastically, and the crack grows. The force-displacement curve predicted by FEM is in good agreement with the experimental study. The maximum force indicated by FEM at the fracture point is almost the same as in the experimental research. The force versus displacement has a linear trend at the start of loading. The softening behavior is observed at a stroke of almost 0.5 mm, and then the force reaches its maximum amount of 0.99 kN at a stroke of 1.22 mm. The maximum force withstood by sample C is almost 11 % higher than that of sample F (the force after the densification point is not considered).

Based on the previous definition, resilience (R) can be defined as the area under the stress-strain curve up to the yield point, so:
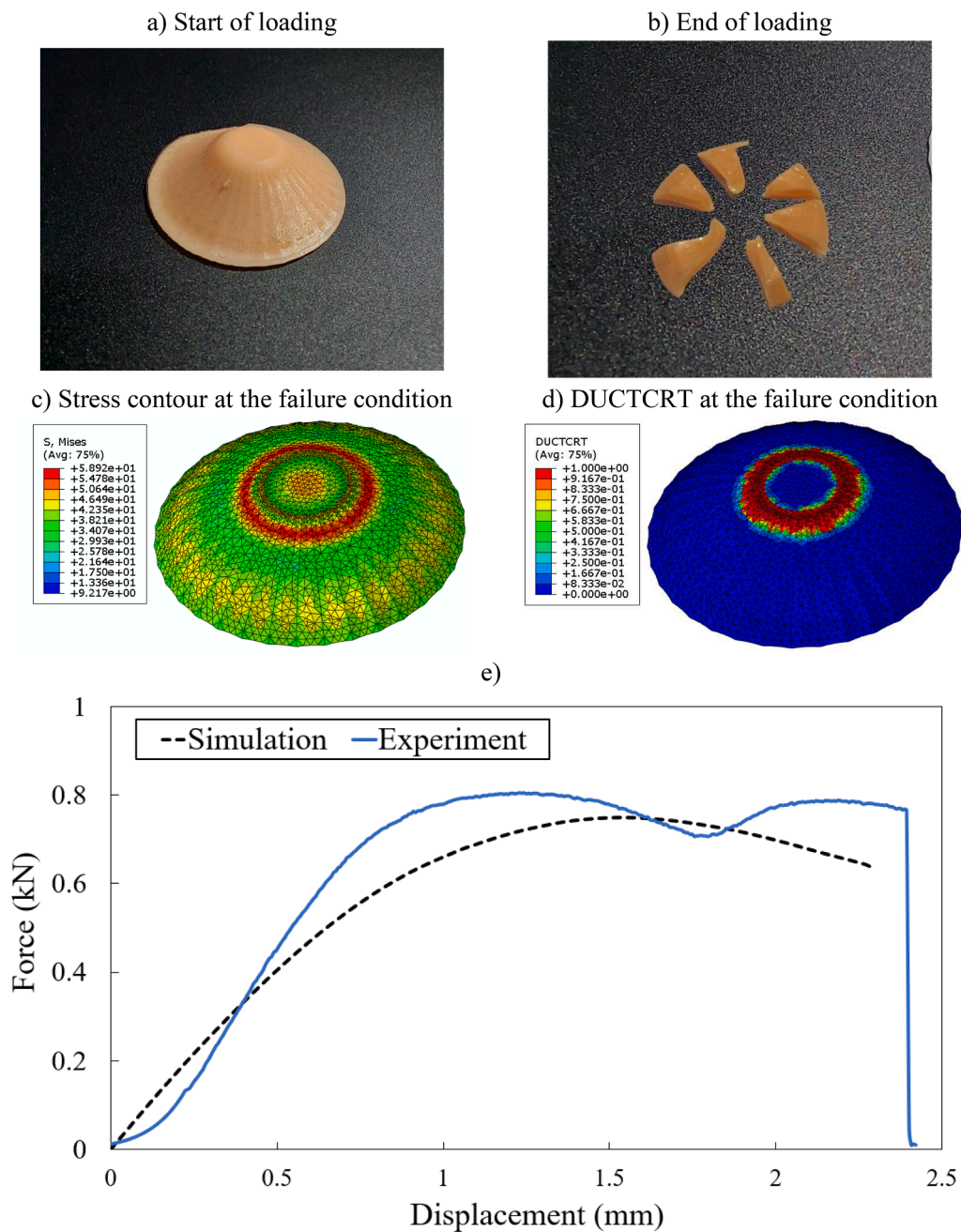
a) Start of loading

b) End of loading

c) Stress contour at the failure condition

d) DUCTCRT at the failure condition

e)

Fig. 13. The counterpart of Fig. 12 for sample E.

$$R = \sigma_y \times \varepsilon_y \qquad (1)$$

In Eq. (1), σ_y, and ε_y stand for resilience, yield stress, and yield strain, respectively. Samples D–F are more resilient than their counterparts (samples A-C, respectively) printed by the FFF technique. Since these structures can absorb more energy than their FFF-printed counterparts until the yield point, they can still return to their original state by unloading. For example, for samples F and C, R equals 2.91 MPa and 1.77 MPa, respectively, so the resilience of sample F is almost 64 % higher than that of sample C.

4.3. Shape recovery feature of PLA printed using FFF technique (recoverability)

PLA, which can be considered a thermoplastic shape memory polymer (SMP), exhibits commendable shape memory characteristics. This material is used in 4D printing technology to provide structure with recoverability. In the current research, samples A-C are printed by employing 4D printing technology. As shown in Fig. 15a, the limpet-inspired shell recovery and the cold programming procedure are elucidated as part of the conceptual design for shape memory.

The shell undergoes loading at ambient temperature, situated below the glass transition temperature, initiating an elastic deformation succeeded by strain-hardening plastic deformation (Step 1). These polymer chains progressively realign in the loading direction, storing mechanical energy. Upon unloading, a swift spring back releases a fraction of the stored energy (Step 2). Meanwhile, the material does not fully revert to its original shape, resulting in residual plastic deformations. Step 3 involves the shape-recovery process, wherein the SMP limpet-shaped shell is heated above T_g (transient temperature), facilitating the restoration of its initial form. Ultimately, cooling the structure to room temperature (RT) results in a complete return to its original shape (see Step 4).
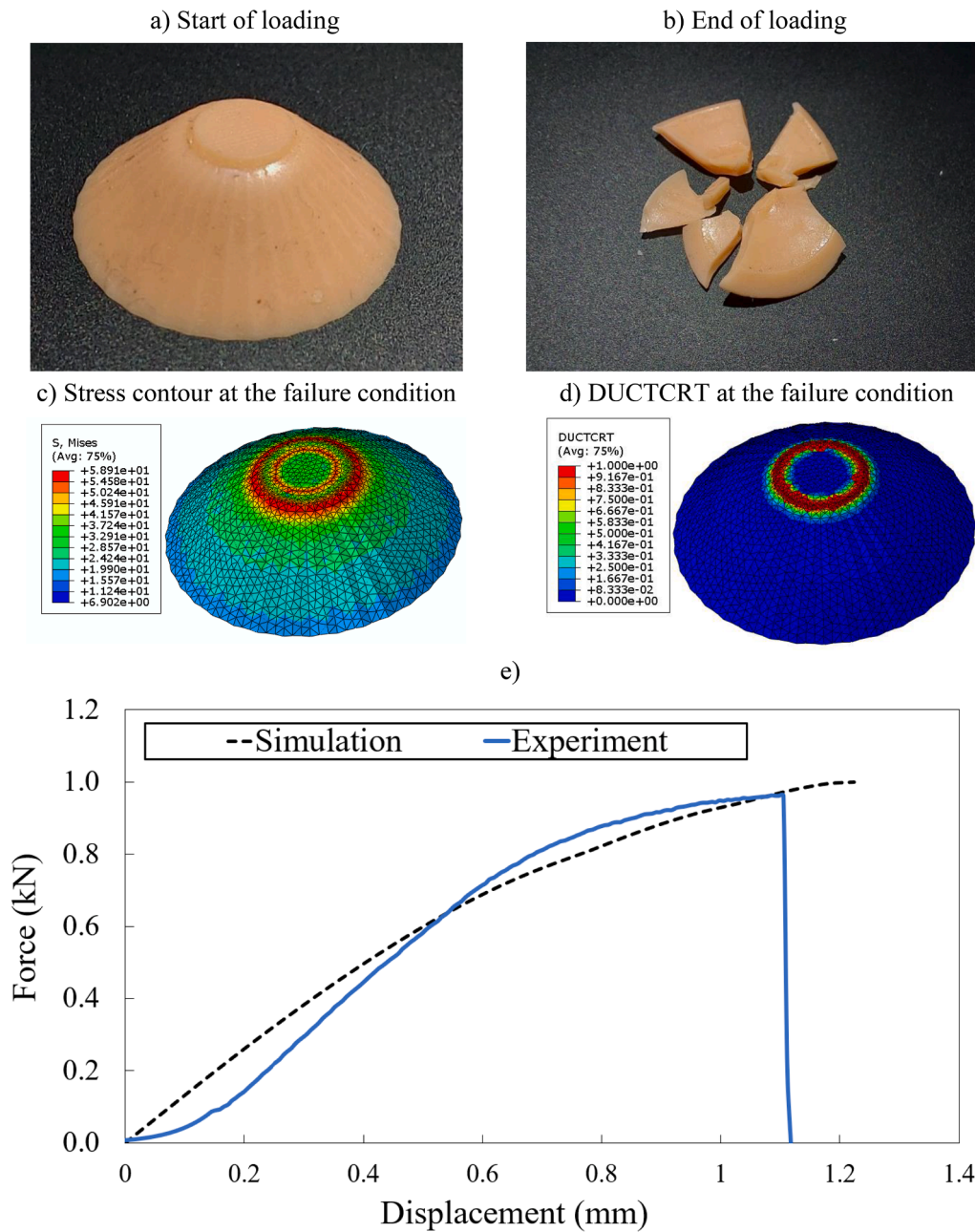
Fig. 14. The counterpart of Fig. 12 for sample F.

Fig. 15b and d show the deformed limpet-inspired unit cells and Fig. 15c and e show the final shape after the heating and cooling process. As shown in Fig. 15c, the structure completely recovers even after a crack is initiated [17].

Fig. 16 illustrates the shape recovery process of sample B for the maximum stroke of 1.8 mm (the strain of 30 %). Fig. 16a illustrates the deformed shape of the unit cell after a stroke of 1.8 mm, and Fig. 16b presents the recovered shape of the structure. The structure is fully recovered after the heating-cooling process. The force-displacement of the whole process from the loading, unloading, and heating processes is illustrated in Fig. 16c. After moving down the upper jaw to a displacement of 1.8 mm, the upper jaw moves upward (unloading), and the structure tends to recover its initial shape. However, due to residual plastic strain, it cannot fully recover. By a simple heating-cooling process, the structure fully recovers its initial shape. The red dashed line presents the heating process.

Moreover, in the present research, two primary factors associated with the shape memory characteristics of PLA limpet-inspired shells are investigated, known as shape fixity and shape recovery rate. Shape fixity evaluates the specimen's capability to retain the temporary deformation during the cold programming process. Conversely, the shape recovery rate presents the material's capacity to revert to its initial shape upon heating. The sample B exhibits a shape fixity of 82 % and a shape recovery rate of almost 100 %, see Fig. 16.

4.4. Sandwich panels

The following section investigates repairable sandwich panels consisting of two upper and lower aluminum skins and a linear arrangement of seven rows of limpet shell unit cells, with each unit cell placed in the opposite direction of the neighboring row to enhance the stability of the structure during deformation. The unit cell distances are set to remain separate and without contact, when bending. This feature enables efficient structure repair, as only the damaged unit cells must be replaced
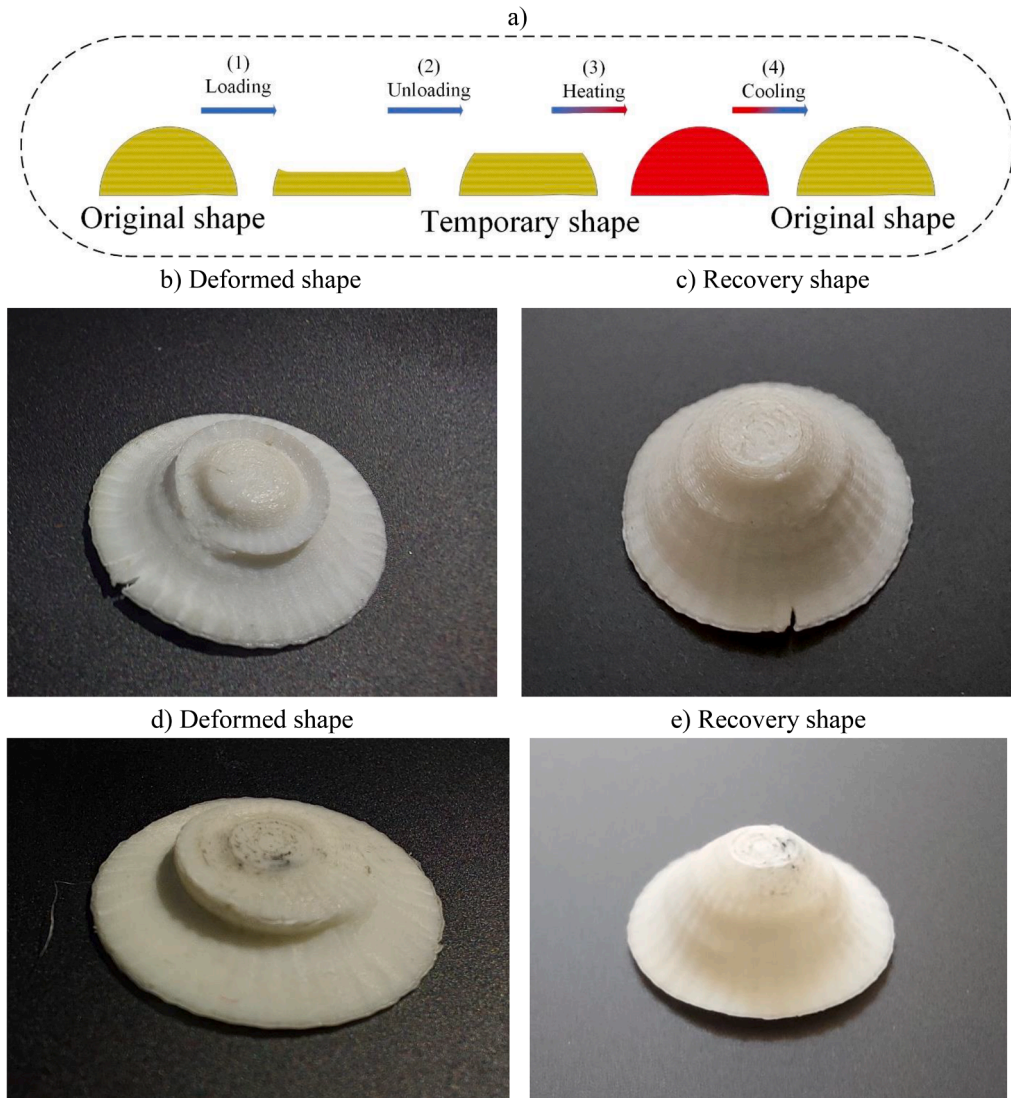
Fig. 15. Shape recovery capability of 3D printed samples using FFF technique.

with intact ones. Considering the samples printed using the FFF technique, samples A and C have the maximum SED (see Section 5.1 for reported samples' SED); meanwhile, sample A is considered for designing sandwich panels to reduce material consumption. The Johnson-Cook model [47] is supposed to model the elastic-plastic behavior of the aluminum A6061-T6 plate, the constants listed in Table 4.

Recently, sustainable sandwich structures using bottle caps due to sustainability, significant flexural strength, and good impact strength attracted attention [37,48–50]. In the present research, sandwich panels with the exact volume of sandwich structures proposed by Oliveira et al. [49] are designed to make a realistic compression between the current design and sustainable sandwich panels based on the bottle caps. The thickness of the aluminum face sheets is 1 mm. The ASTM C393 standard is used to design the sandwich structures, so the sandwich panels' length and width are 246.5 mm and 91.5 mm, respectively followed by Oliveira et al. [49].

Fig. 17a shows the designed sandwich panels with aluminum face sheets and 21 designed limpet shells; the final dimensions are 246.5 mm × 91.5 mm × 13.5 mm. The unit cells are scaled nearly by 2 to create the sandwich panels with the same volume as Olivera et al.'s design with bottle caps. The same trend for SED is observed by scaling the samples according to finite element analysis of the scaled limpet shell, meaning

scaled sample E has the maximum SED compared to scaled samples D and F. As shown in Fig. 17a, unit cells are placed so that the minimum number of limpet shells are used while covering the maximum area of the aluminum skins and maintaining no contact between unit cells during deformation. Fig. 17b is Oliveira et al.'s structure, which introduced a sustainable sandwich panel made from aluminum skins and 24 recycled thermoplastic bottle cap cores. The final dimension of their structure is 246.5 mm × 91.5 mm × 13.5 mm. The three-point bending test is conducted on the designed sandwich panels in the present research and compared with Olivera et al. results.

Fig. 18 presents the results for three-point bending for sandwich structures of type A, sandwich structures with aluminum face sheets, and 21 FFF limpet unit cells. Unit cells are the same as in sample A, scaled nearly by 2 for the sandwich panels type A with the same H/L ratio. The three-point bending configuration of sandwich structure type A is depicted in Fig. 18a. Fig. 18b and c illustrate von Mises' stress contour for aluminum skins and cores, respectively, for strokes of 10 mm. The von Mises stress ranges from 0.02 MPa to 271.50 MPa in the aluminum face sheets, while in the unit cell, it ranges from 0.06 MPa to 43.99 MPa. As shown in Fig. 18c, the maximum stress occurs in the middle of panels; meanwhile, the unit cells on the edge of structures are subjected to fewer compression loads compared to the unit cells in the middle.
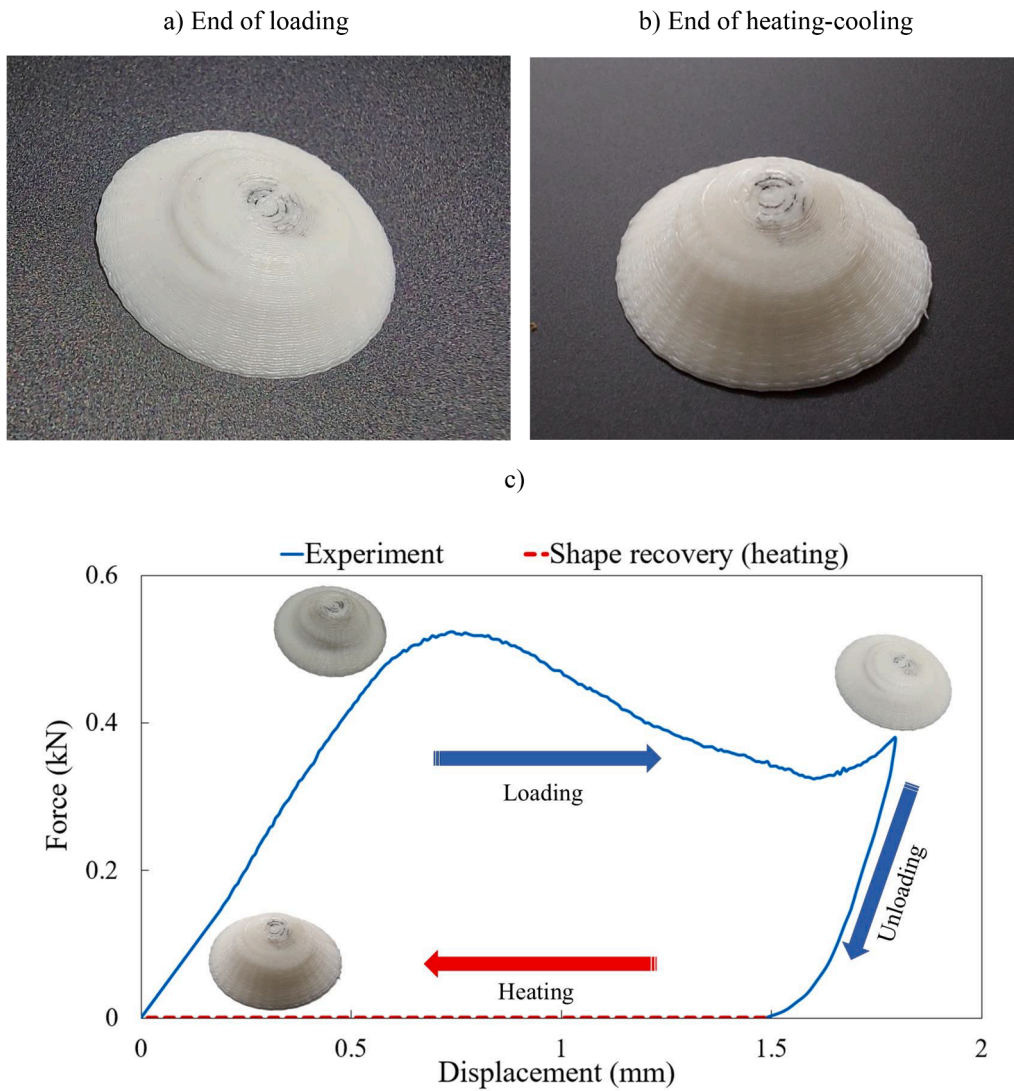
a) End of loading   b) End of heating-cooling

c)

Fig. 16. Shape recovery process of sample B (a) deformed form after strain of 30 %, (b) recovery of sample, and (c) force-displacement process of sample B.

Table 4
Johnson-Cook model constants of Al6061-T6 [47].

A (MPa)	B (MPa)	C_0	n	m_0
324	114	0.002	0.42	1.34

Fig. 19 presents results for three-point bending for sandwich structures of type B, sandwich structures with aluminum face sheets, and 21 LCD limpet shell unit cells of sample E. Unit cells are the same as sample E, scaled by 2 for the sandwich panels type B with the same H/L ratio. The three-point bending configuration of sandwich structure type B is depicted in Fig. 19a for the stroke of 10 mm. Fig. 19b and c illustrate von Mises stress contour for aluminum skins and cores. The von Mises stress ranges from 0.07 MPa to 262.80 MPa in the aluminum face sheets, while in the unit cell, it ranges from 0.07 MPa to 58.91 MPa. As shown in Fig. 19c, the maximum stress occurs in the middle of the structure; meanwhile, the unit cells on the edge of the structure are subjected to fewer compression loads compared to the unit cells in the middle. Finally, Fig. 19d shows the DUCTCRT for unit cells to present the failure location clearly. Fractures occurred in the three middle unit cells after 10 mm displacement, which can be replaced by intact ones after damage.

Fig. 20 displays the force-displacement diagram of the sandwich

panel types A and B (present research) and Oliveira's research [49] for sandwich panels with cubic packing for the adhesive thickness of 0.8 mm, named type A, and the adhesive thickness of 1.5 mm, named type B. Results show the maximum force withstandable by sandwich structures types A and B is 3.41 kN and 3.80 kN, respectively, almost the same for both designs. However, the maximum force withstandable by sandwich structure types A and B designed by Oliveira et al. [49] is 1.15 kN and 2.13 kN, respectively. Moreover, Table 5 compares the energy dissipation per unit mass for all designs. Oliveira et al. [49] do not report the mass of sandwich panels, so the mass is calculated based on the average mass of bottle caps, aluminum, and adhesive in the current research to make a meaningful compression. It is worth mentioning that details related to calculateing SED is defined in Section 5.1.

According to Table 5, the sandwich panel type A exhibits a higher specific energy dissipation per unit mass, 0.50 J/g, compared to all samples. Furthermore, it has almost 7.33 and 1.17 times higher SED than sandwich panels type A and B, designed by Oliveira et al. Table 5 shows that the proposed design in the present research has high energy dissipation per unit mass, making them potential energy absorption/dissipation structures for future applications regarding both energy absorption/dissipation and mass reduction.
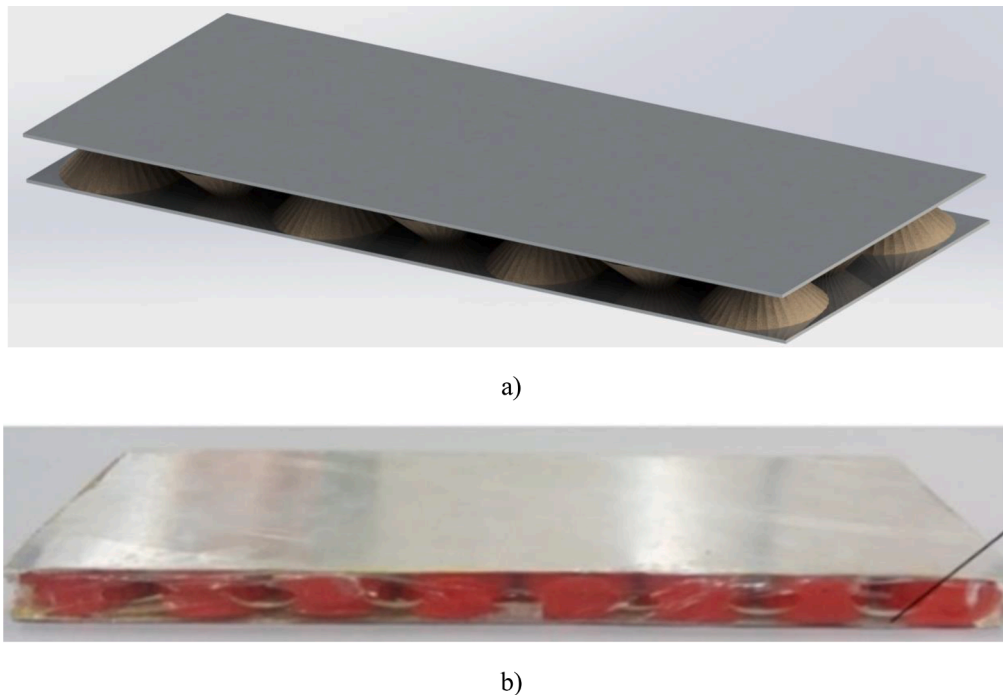
Fig. 17. Standard structures: (a) A sandwich panel with Aluminum face sheets and 21 designed limpet shells. The final dimensions are 246.5 × 91.5 × 13.5 mm. (b) Oliveira et al.'s structure (they introduced a sustainable sandwich panel made from aluminum skins and a recycled thermoplastic bottle cap core [49]).

5. Discussion

5.1. Energy absorption capability of bio-inspired limpet shells

The area delineated by the loading and unloading curves defines the energy dissipation, primarily attributed to plastic deformations and mechanical instability. The input energy due to the applied force is transformed into kinetic energy, and some of it is dissipated via instability and the plastic deformation mechanism. The absorbed energy attributed to elastic deformations is computed based on the area beneath the unloading curve. In the present research, loading is applied until the densification happens. So, in order to calculate the dissipated energy in sample A-C, the tangent line is drawn at the start of densification and intercepts with the displacement axis; the region contained this line, and a force-displacement curve is considered to be dissipated energy, as shown in Fig. 21.

The force-displacement behavior of structures manufactured by elastic-plastic material experiencing substantial deformation manifests in three stages. In the initial linear elastic stage, shells undergo simple elastic bending. The subsequent plateau stage is influenced by three potential failure mechanisms of components: elastic buckling, plastic collapse, or brittle fracture. The concluding stage, characterized by densification, witnesses a sharp increase in force corresponding to the applied displacement. The plateau stage contributed significantly to the energy dissipation capability of structures [17]. For samples D–F, the dissipation energy is the region under the force-displacement curve as the fracture happened, and almost all the input energy dissipated.

Recently, emphasis has been placed on reducing mass in engineering structures, prompted by concerns surrounding fossil fuel consumption and environmental challenges. Consequently, in the sustainable design of sandwich structures for energy absorption/dissipation applications, consideration must be given to both energy absorption/dissipation and the overall mass. The focus here is on the term specific energy dissipation (SED), which denotes energy dissipation per unit mass. This perspective is explored per the findings of Yousefi et al. [18], which is defined as:

$$SED = \frac{Energy\ dissipation}{Structure\ mass} \tag{2}$$

Table 6 lists the structure mass, energy dissipation, and specific energy dissipation per unit mass for all samples. For samples A-C, printed by the FFF technique, sample A has the maximum SED, almost the same as sample C. So, results show that by increasing the thickness of the unit cell and consuming a higher volume of materials, the SED decreases. Samples A and C have SED, almost 31 % higher than sample B. Results emphasize the geometry optimization of unit cells, especially nowadays, when the world is attempting to reduce fuel consumption. As samples A and C have almost the same SED, sample A is proposed for future applications such as designing sandwich panels, as sample A consumes less materials compared to sample C by nearly 61 % while having the same SED.

For samples D–F, samples printed by the LCD technique, sample E, which has a geometry close to natural limpet, has the maximum SED. As discussed earlier, the samples printed using the LCD technique have the material's behavior close to limpet; the fracture happens with smaller plastic deformation and has brittle properties. This is an exciting result since for a sample with material that has mechanical behavior close to the natural limpet, the sample with the same geometry as the natural limpet (sample E) has the maximum energy dissipation per unit mass. The SED of sample E is 494 % and 189 % higher than samples D and F, respectively.

5.2. Bio-Inspiring design and its benefit

Limpets employ a strong, rigid calcium carbonate shell as a defensive mechanism, serving multiple purposes, such as deterring predators, minimizing water loss during low tide exposure, and offering protection against physical impacts. Impact events stemming from storms and stones, debris, and ice thrown by waves pose significant challenges [44, 51,52]. The limpet's shell formation, growth, and sustainment entail substantial energy expenditure. This issue is the same as designing a structure, such as a sandwich structure, to safeguard against impact while maintaining a relatively lightweight profile [52].
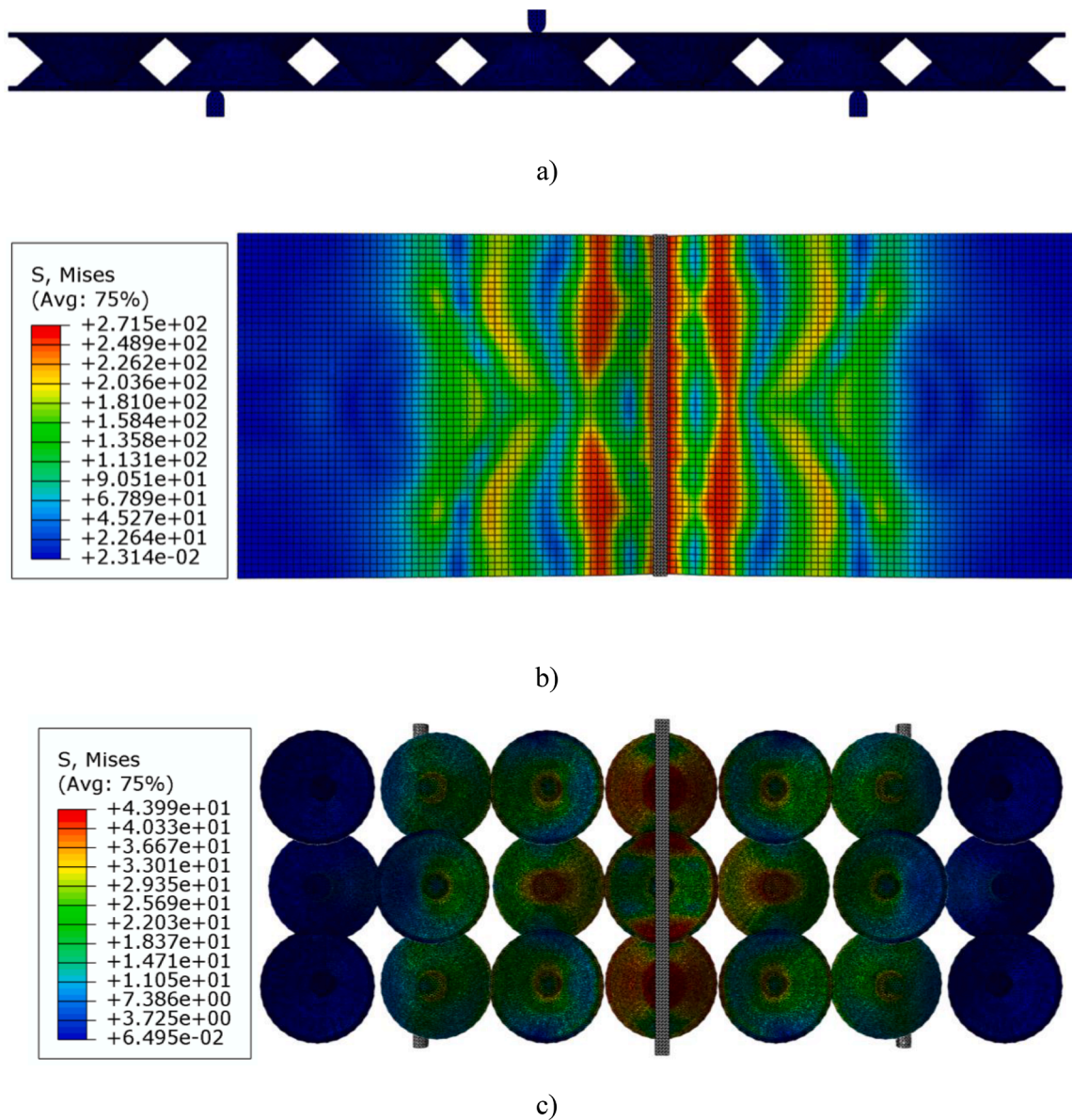
Fig. 18. (a) Designed standard structure with sample A, (b) the distribution of von Mises stress in aluminum skins, (c) the distribution of von Mises in stress analysis in unit cells.

Interestingly, Harford et al. [52] show that limpets have developed two strategies to modulate the impact strength of their shells. Initially, they can alter the height-to-length aspect ratio (H/L) by making the shell tall or short with a flatter bottom surface. Additionally, limpets can independently manipulate the thickness of the shell near the apex. Those located in a narrow fissure, especially in rocks characterized by a lower likelihood of impacts, exhibit a thinner shell. In the present study, based on the excellent ability of limpet to adapt to impact, a novel design is developed to employ in a sandwich panel, enhancing the energy dissipation capability of the sandwich panel. It is worth mentioning that the proposed design can be used in other structures with energy absorption applications.

As discussed before, due to the simplicity of the design and its high energy dissipation capability, the proposed design can be manufactured using different manufacturing techniques. Therefore, the current bio-inspired design can be manufactured using other materials; for example, it can be made of cast iron and manufactured using casting techniques. This unique feature makes the proposed design even more viable for energy dissipation applications in industries.

In the marine industry, boat fenders are highly crucial for the boats; they absorb the impact energy during the berthing; indeed, the boat fenders have the same function as the car bumper [17]. The impact force during the berthing is destructive, so the boat fender must have high energy absorption capability to negate or reduce the impact consequences. The present design can be employed to design and develop novel types of boat fenders. Moreover, a novel conceptual design for a new class of lightweight boat fenders is introduced in that if one of the unit cells fails, this unit cell can be replaced by a new one. There is no need to replace all the boat fender structures. Another possible application can be inside the helmet, where energy absorption/dissipation is also essential.

5.3. Repairability or design for repair

The sandwich panels presented in this research have a unique feature: the core can be replaced after being damaged by an intact one. Hedayati et al. [22] proposed a sandwich structure with an easy-to-repair 3D-printed truncated cube core for the first time. In the
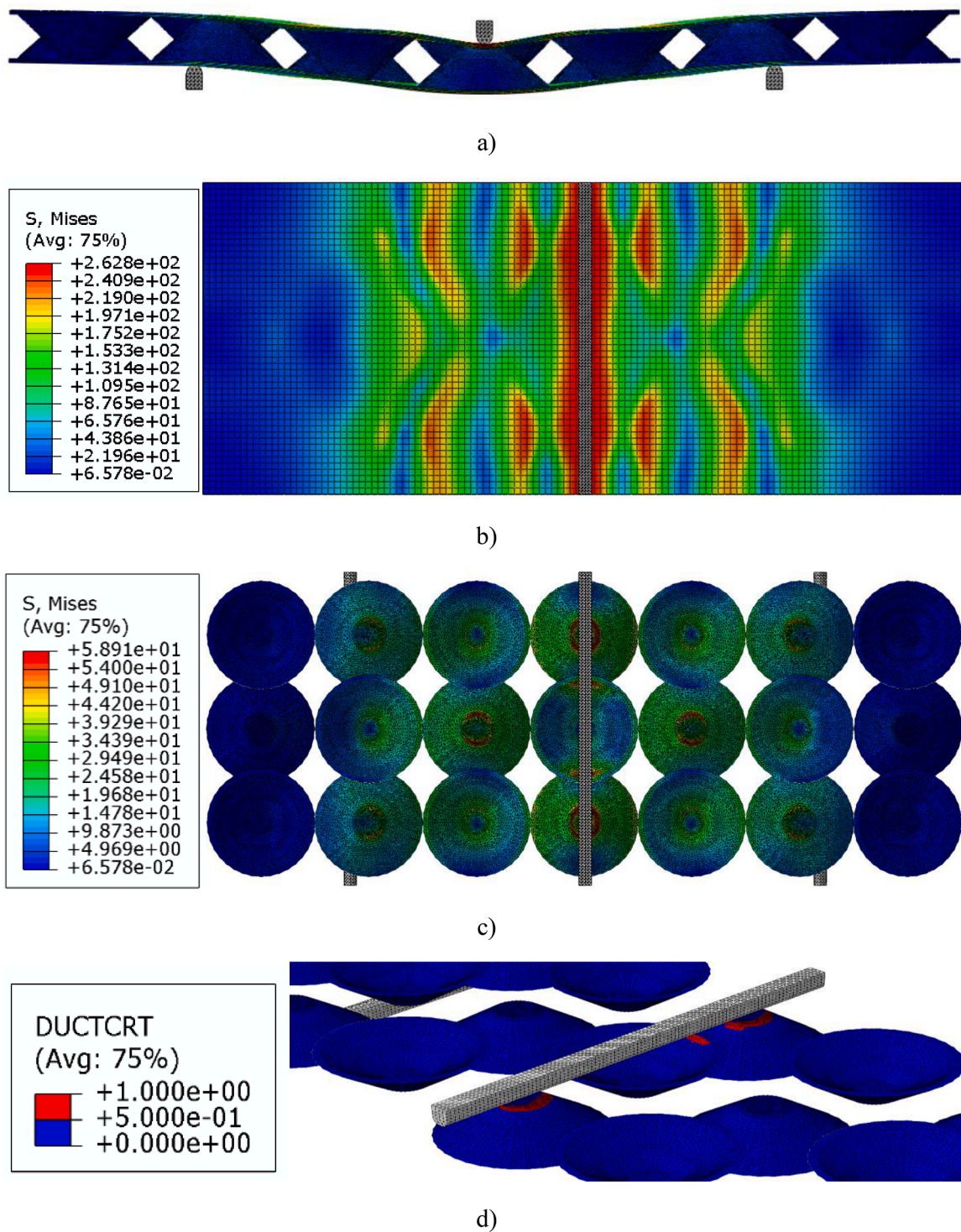
a)

b)

c)

d)

Fig. 19. (a) Designed standard structure with sample E, (b) the distribution of von Mises stress in aluminum skins, (c) the distribution of von Mises stress in unit cells, and (d) DUCTCRT at the failure condition in unit cells.

current research, the sandwich structure with limpet-inspired unit cells as the core is proposed, in which, because of the unique core design, the damaged unit cells can be easily repaired. Consequently, replacing the entire structure is not imperative, leading to reduced maintenance costs. The use of separated unit cells as the core for sandwich panels enables the facile replacement of damaged units. Designing sandwich panels with repairable cores employing conventional lattice is not economical or easy to manufacture.

As discussed, two methods of 3D printing are used; each result in

selected material properties, and each has some advantages. Sandwich panel type A, manufactured by 3D printed PLA limpet-shaped, can withstand more considerable deformation than sandwich panel type B. The energy dissipation per unit mass capability of sandwich panel type A is higher than that of sandwich panel type B. The sandwich panel type A has shape recovery properties; after deforming, the structure can recover its initial form by simply heating. Sandwich panel type B, subjected to bending after the fracture of the unit cell, does not tend to move back, so all absorbed energy is dissipated after the fracture. While the sandwich
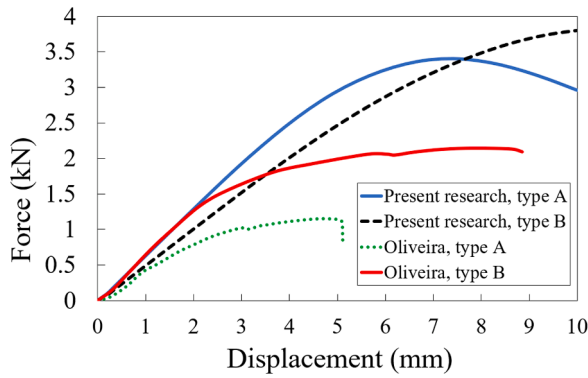
Fig. 20. Force-displacement diagram of the standard structures in the current study and Oliveira et al.'s structure [49].

Table 5
The energy dissipation and SED for all samples.

Sample type	m (g)	Energy dissipation (J)	SED (J/g)
Standard panel type A	48.15	24.03	0.50
Standard panel type B	49.35	22.64	0.46
Oliveira et al.'s type A	61.97	4.03	0.06
Oliveira et al.'s type B	61.99	14.45	0.23

panel type A has spring-like mechanical behavior, when compression load is removed, the structure tends to recover a portion of its initial shape due to absorbed energy.

In the present research, the concept of a sandwich structure with a repairable core was investigated numerically, in order for real-world applications the structures should be manufactured and the mechanical behavior of the structure should be investigated experimentally. However, using FEM software, ABAQUS, and CAD software, SOLID-WORKS, also simulates a three-point bending test, demonstrating that by selecting the proper distance between limpet-inspired shells, and proper numbers of shells based on the dimensions of sandwich panels, the recoverability can be achievable.

5.4. Application in boat fender

As discussed in Section 5.1, compared to alternative unit cell types, the limpet-inspired unit cell offers a diverse range of mechanical properties, such as significant energy dissipation capability, a critical parameter in the design of sandwich structures. The proposed core unit cells, which can be located upward and downward, sustain a substantial contact area with the upper and lower aluminum plates at the interface, ensuring high stability during deformation and a heightened energy absorption capability. Also, the proposed design can be employed to develop a new type of recoverable boat fender with an easy-to-repair capability.

In order to examine the applicability of limpet-inspired design for boat fender applications, the Fender Application Design Manual [53] is
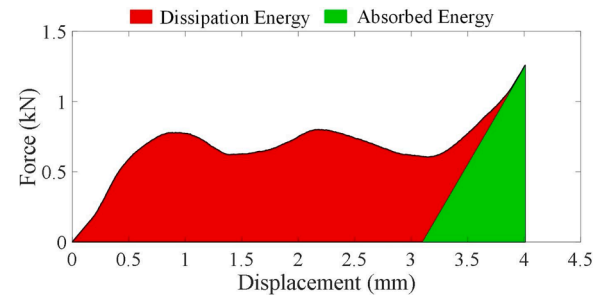

Fig. 21. The energy distribution is based on the force-displacement curve.

Table 6
The energy absorption and SED for all samples.

Sample type	m (g)	Energy dissipation (J)	SED (J/g)
Sample A	0.308	1.550	5.032
Sample B	0.407	1.570	3.857
Sample C	0.495	2.492	5.034
Sample D	0.251	0.190	0.757
Sample E	0.332	1.494	4.500
Sample F	0.404	0.630	1.559

employed. According to [53], the normal berthing energy is crucial for designing the boat fender. Normal berthing energy is defined as:

$$E_N = 0.5 \times M_D \times V_B{}^2 \times C_M \times C_E \times C_C \times C_S \tag{3}$$

where,

$E_N =$ Normal berthing energy to be absorbed by the fender (J)
$M_D =$ Mass of the boat
$V_B =$ Approach velocity component perpendicular to the berthing line (m/s)
$C_M =$ Added mass coefficient
$C_E =$ Eccentricity coefficient
$C_C =$ Berth configuration coefficient
$C_S =$ Softness coefficient

By assuming that the limpet-inspired design is used for a deck boat fendering system, according to [53]:
C_m depends on the boat's geometry, for a deck boat, it is close to $C_m = 0.6$.
For the soft fender, the same as the present design, $C_s = 1$.

$$M_D = \text{LWT} + \text{DWT} = 1500 + 500 = 2000 \text{ kg}$$

LWT stands for boat weight, and DWT stands for the weight of cargo and crew. Slide berthing is the most common type of berthing, although there are other types. According to [53], in the case of good berthing and for normal boats, $V_B = 0.1$ m/s. The worst-case scenario involves challenging berthing (sheltered) with $V_B = 0.35$ m/s, and $C_E = 1$ that induced a higher amount of energy to the fendering system, which is considered in the present research.

The berth configuration coefficient (C_c) is defined as the energy dissipated by water during berthing. In the present project, it is assumed that the case is closed form, so $C_c = 0.9$.

So the normal berthing energy to be absorbed by the boat fender is $E_N = 66.15$ J

During the berthing, 66.15 J must be carried out using a well-

designed boat fender. According to Table 6, sample C can dissipate, 2.492 J, although in order to manufacture a fendering system, arrays of sample C can be used. For example, as the dimension of sample C is small (the outer diameter is 18 mm), 100 of sample C can be used which can dissipate almost 249.2 J, 2.77 times higher than the energy induced by berthing, so the proposed design is feasible.

6. Summary and concluding remarks

Considering the limpet's high energy dissipation capability, the present research has developed a bio-inspired design based on the limpet geometry. Two AM techniques were employed to fabricate limpet-inspired shells with different materials and mechanical behaviors. The compression test was conducted on the shells to determine the force-displacement curve for all samples. A FEM employing ABAQUS software and considering an elastic-plastic materials model was developed to calculate force-displacement for all samples. Following the energy dissipation, the SED was reported for all samples. The optimized design considering energy dissipation per mass of the structure was selected, and the sandwich structure with repairable cores was developed. According to the ASTM C393 standard, the three-point bending test was simulated using ABAQUS. The force-displacement curves and the energy dissipation of panels were reported. The following main results from the present research can be concluded:

- The maximum force withstood by sample A is 160 % higher than sample D, which has the same geometry but different mechanical properties.
- The maximum force withstood by sample E is 60 % higher than sample B, which has the same geometry but different mechanical properties.
- The maximum force withstood by sample C is almost 11 % higher than that of sample F, the sample with the same geometry but different mechanical properties.
- Samples D–F are more resilient than their counterpart (with the same geometry) printed by the FFF method; for example, the resilience of sample F is almost 64 % higher than that of sample C.
- The bio-inspired design shows excellent energy dissipation capability
- For samples A–C, which are printed using the FFF technique, samples A and C have SED, almost 31 % higher than sample B.
- For samples D–F, printed using the LCD technique, a sample with material with mechanical behavior close to the natural limpet and the same geometry as the natural limpet (sample E) has a maximum SED, almost 494 % higher than sample D and 189 % higher than sample F.
- Samples A-C, printed using the FFF technique, can recover their original shape just by heating them.
- Sandwich panels with bio-inspired core (limpet-inspired shell) demonstrate repairability, in which if one of the unit cells is damaged, it can be easily replaced by an intact one.
- Sandwich panel type A can recover its initial shape by simple heating, possessing both recoverability and repairability.
- The sandwich panel type A has the maximum SED, almost 7.33 and 1.17 times higher SED than sandwich panel types A and B, designed by Oliveira et al. [49].

The recoverable, energy-dissipating, limpet-inspired shell with supreme resilience proposed in this work could be instrumental in designing lightweight sandwich panels with easy-to-repair features. They could have a wide range of applications in various industries like aerospace (e.g., landing gears, aerial vehicle body), automotive (e.g., car bumper, car body), marine (e.g., boat fender), sport (e.g., protective gears, helmet), and healthcare (e.g., flooring in care home) promoting sustainability.

CRediT authorship contribution statement

Saman Jolaiy: Writing – original draft, Visualization, Validation, Methodology, Investigation, Formal analysis, Data curation, Conceptualization. **Armin Yousefi:** Writing – original draft, Visualization, Validation, Methodology, Investigation, Formal analysis, Conceptualization. **Mohsen Hosseini:** Writing – original draft, Visualization, Investigation, Data curation. **Ali Zolfagharian:** Writing – review & editing, Methodology, Investigation, Formal analysis. **Frédéric Demoly:** Writing – review & editing, Visualization, Methodology, Investigation, Formal analysis. **Mahdi Bodaghi:** Writing – review & editing, Supervision, Resources, Project administration, Methodology, Investigation, Funding acquisition, Formal analysis, Data curation, Conceptualization.

Declaration of competing interest

The authors declare that they have no known competing financial interests or personal relationships that could have appeared to influence the work reported in this paper.

Data availability

The raw/processed data required to reproduce these findings will be made available upon request from the corresponding author.

Acknowledgment

References

[1] S. Kamarian, M. Bodaghi, J.i. Song, Hygrothermal effects on the buckling of soft-core sandwich plates with composite layered face sheets, Polym. Compos. 41 (10) (2020) 4144–4169.

[2] M. Safarabadi, et al., Experimental and numerical study of buckling behavior of foam-filled honeycomb core sandwich panels considering viscoelastic effects, J. Sandw. Struct. Mater. 23 (8) (2021) 3985–4015.

[3] M. Mehrpouya, et al., Investigation on shape recovery of 3D printed honeycomb sandwich structure, Polym. Adv. Technol. 31 (12) (2020) 3361–3365.

[4] H.Y. Sarvestani, et al., 3D printed architected polymeric sandwich panels: energy absorption and structural performance, Compos. Struct. 200 (2018) 886–909.

[5] X. Bai, Z. Zheng, A. Nakayama, Heat transfer performance analysis on lattice core sandwich panel structures, Int. J. Heat Mass Transf. 143 (2019) 118525.

[6] M. Proença, et al., Acoustic performance of composite sandwich panels for building floors: experimental tests and numerical-analytical simulation, J. Build. Eng. 32 (2020) 101751.

[7] A. Akbarzadeh, et al., Dynamic eigenstrain behavior of magnetoelastic functionally graded cellular cylinders, Compos. Struct. 116 (2014) 404–413.

[8] Z. Zhang, et al., Out-of-plane compressive performance and energy absorption of multi-layer graded sinusoidal corrugated sandwich panels, Mater. Des. 178 (2019) 107858.

[9] N.S. Ha, G. Lu, X. Xiang, Energy absorption of a bio-inspired honeycomb sandwich panel, J. Mater. Sci. 54 (2019) 6286–6300.

[10] A. Farrokhabadi, et al., Experimental and numerical analysis of novel multi-layer sandwich panels under three point bending load, Compos. Struct. 250 (2020) 112631.

[11] B. Chen, et al., Multifunctional cellular sandwich structures with optimised core topologies for improved mechanical properties and energy harvesting performance, Compos. Part B Eng. 238 (2022) 109899.

[12] E.C. Clough, et al., Mechanical performance of hollow tetrahedral truss cores, Int. J. Solids Struct. 91 (2016) 115–126.

[13] J. Liu, et al., The edgewise compressive behavior and failure mechanism of the composite Y-frame core sandwich column, Polym. Test. 81 (2020) 106188.

[14] S. Alsubari, et al., Effect of foam filling on the energy absorption behaviour of flax/polylactic acid composite interlocking sandwich structures, Compos. Struct. 292 (2022) 115685.

[15] Y. Zhang, et al., Static and dynamic crushing responses of CFRP sandwich panels filled with different reinforced materials, Mater. Des. 117 (2017) 396–408.

[16] H.N.G. Wadley, et al., Impact response of aluminum corrugated core sandwich panels, Int. J. Impact Eng. 62 (2013) 114–128.

[17] M. Bodaghi, et al., Metamaterial boat fenders with supreme shape recovery and energy absorption/dissipation via FFF 4D printing, Smart Mater. Struct. 32 (2023) 095028.

[18] A. Yousefi, et al., 3D-printed soft and hard meta-structures with supreme energy absorption and dissipation capacities in cyclic loading conditions, Adv. Eng. Mater. 25 (4) (2023) 2201189.

[19] R. Hedayati, et al., Analytical relationships for 2D *Re*-entrant auxetic metamaterials: an application to 3D printing flexible implants, J. Mech. Behav. Biomed. Mater. 143 (2023) 105938.

[20] R. Akman, et al., Multimodal 3D printing of biodegradable shape memory elastomer resins for patient specific soft tissue repair, Appl. Mater. Today 29 (2022) 101666.

[21] A. Serjouei, et al., 4D printed shape memory sandwich structures: experimental analysis and numerical modeling, Smart Mater. Struct. 31 (5) (2022) 055014.

[22] R. Hedayati, A. Yousefi, M. Bodaghi, Sandwich structures with repairable cores based on truncated cube cells, Compos. Part B Eng. 243 (2022) 110124.

[23] R. Hamzehei, et al., 4D metamaterials with zero poisson's ratio, shape recovery, and energy absorption features, Adv. Eng. Mater. 24 (9) (2022) 2200656.

[24] M. Bodaghi, et al., Reversible energy absorbing meta-sandwiches by FDM 4D printing, Int. J. Mech. Sci. 173 (2020) 105451.

[25] X. Liu, et al., 4D printing of butterfly scale–inspired structures for wide-angle directional liquid transport, Small 19 (34) (2023) 2207640.

[26] B.C. Kholkhoev, et al., 4D-printing of mechanically durable high-temperature shape memory polymer with good irradiation resistance, Appl. Mater. Today 36 (2024) 102022.

[27] T. Gu, et al., 4D printed and multi-stimulus responsive shape memory polymer nanocomposites developed on hydrogen bonding–metal-phenolic sacrificial network: application for hazardous chemical operations soft robots, Appl. Mater. Today 35 (2023) 102009.

[28] K. Hu, et al., Mechanical properties and deformation behavior under compressive loading of selective laser melting processed bio-inspired sandwich structures, Mater. Sci. Eng. A 762 (2019) 138089.

[29] G. Thomas, V. Keller, D. Spitzer, Highly vertical 3D bio-inspired hierarchical and multiscale superstructures on microcantilever for gas sensing of organophosphorous agents, Appl. Mater. Today 29 (2022) 101667.

[30] Z. Zhang, et al., Bamboo-inspired, simulation-guided design and 3D printing of light-weight and high-strength mechanical metamaterials, Appl. Mater. Today 26 (2022) 101268.

[31] M. Mirkhalaf, et al., Toughness by segmentation: fabrication, testing and micromechanics of architectured ceramic panels for impact applications, Int. J. Solids Struct. 158 (2019) 52–65.

[32] K. Yokota, F. Barthelat, Stiff bioinspired architectured beams bend Saint-Venant's principle and generate large shape morphing, Int. J. Solids Struct. 274 (2023) 112270.

[33] L. Meng, et al., Failure analysis of bio-inspired corrugated sandwich structures fabricated by laser powder bed fusion under three-point bending, Compos. Struct. 263 (2021) 113724.

[34] C. Peng, et al., 3D printed sandwich beams with bioinspired cores: mechanical performance and modelling, Thin Walled Struct. 161 (2021) 107471.

[35] A. Kueh, Y. Siaw, Impact resistance of bio-inspired sandwich beam with side-arched and honeycomb dual-core, Compos. Struct. 275 (2021) 114439.

[36] M. Gunasegeran, et al., Investigation of quasi-static indentation on sandwich structure with GFRP face sheets and PLA bio-inspired core: numerical and experimental study, Thin Walled Struct. 184 (2023) 110501.

[37] P.R. Oliveira, et al., Bio-based/green sandwich structures: a review, Thin Walled Struct. 177 (2022) 109426.

[38] C. Cui, et al., Compressive resistance of the bio-inspired cuttlebone-like sandwich structure under quasi-static load, Int. J. Mech. Sci. 248 (2023) 108222.

[39] V.T. Le, T. Jin, N.S. Goo, Mechanical behaviors and fracture mechanisms of CFRP sandwich composite structures with bio-inspired thin-walled corrugated cores, Aerosp. Sci. Technol. 126 (2022) 107599.

[40] D. Taylor, Impact damage and repair in shells of the limpet Patella vulgata, J. Exp. Biol. 219 (24) (2016) 3927–3935.

[41] J.E. Ortiz, et al., Protein diagenesis in Patella shells: implications for amino acid racemisation dating, Quat. Geochronol. 27 (2015) 105–118.

[42] H. Zhang, et al., Preparation of nacre-like composites by reactive infiltration of a magnesium alloy into porous silicon carbide derived from ice template, Mater. Lett. 183 (2016) 299–302.

[43] D. Vafidis, et al., Population characteristics of the limpet Patella caerulea (Linnaeus, 1758) in Eastern Mediterranean (Central Greece), Water 12 (4) (2020) 1186.

[44] M. O'Neill, et al., Fracture toughness and damage development in limpet shells, Theor. Appl. Fract. Mech. 96 (2018) 168–173.

[45] M. Kolmann, et al., Morphology does not predict performance: jaw curvature and prey crushing in durophagous stingrays, J. Exp. Biol. 218 (24) (2015) 3941–3949.

[46] M. Bazyar, et al., A novel practical method for the production of functionally graded materials by varying exposure time via photo-curing 3D printing, J. Manuf. Process. 103 (2023) 136–143.

[47] S. Akram, et al., Numerical and experimental investigation of Johnson–Cook material models for aluminum (Al 6061-T6) alloy using orthogonal machining approach, Adv. Mech. Eng. 10 (2018) 1–14.

[48] P.R. Oliveira, et al., Eco-friendly sandwich panel based on bottle caps core and sustainable components: static and dynamic characterisation, Compos. Part C Open Access 3 (2020) 100069.

[49] P.R. Oliveira, et al., Sustainable sandwich structures made from bottle caps core and aluminium skins: a statistical approach, Thin Walled Struct. 130 (2018) 362–371.

[50] P.R. Oliveira, et al., Improved sustainable sandwich panels based on bottle caps core, Compos. Part B Eng. 199 (2020) 108165.

[51] G.C. Cadée, Shell damage and shell repair in the Antarctic limpet Nacella concinna from King George Island, J. Sea Res. 41 (1–2) (1999) 149–161.

[52] N. Harford, N. O'Connor, D. Taylor, Impact resistance of limpet shells: a study of local adaptations, Appl. Phys. A 126 (2020) 1–9.

[53] Infrastructure, T.M.A., Fender application design manual, 2022, (Trelleborg) (available at: https://www.trelleborg.com/marine-and-infrastructure/-/media/marine-systems/resources/guides-and-design-manual/downloads/fender-application-design-manual.pdf?rev=f3e34525d9ee4331b058f46f0ec489f4).